SAND79-1673
UNLIMITED RELEASE

PRODUCTION AND POST-ACCELERATION OF INTENSE ION BEAMS IN MAGNETICALLY INSULATED GAPS

S. Humphries, Jr., J. R. Freeman, J. Greenly,*
G. W. Kuswa, C. W. Mendel, J. W. Poukey and
D. W. Woodall**

Sandia Laboratories

SAND77-1673

Category UC-21

Unlimited Release

PRODUCTION AND POST-ACCELERATION OF INTENSE ION BEAMS IN MAGNETICALLY INSULATED GAPS†

S. Humphries, Jr., J. R. Freeman, J. Greenly,* G. J. Kuswa, C. W. Mendel, J. W. Poukey and D. W. Woodall**

*Laboratory of Plasma Studies, Cornell University, Ithaca, NY.

**Department of Chemical and Nuclear Engineering, University of New Mexico, Albuquerque, NM.

†This work was supported by the U. S. Department of Energy, under Contract DE-AC04-76-DP00789.

TABLE OF CONTENTS

PRODUCTION AND POST-ACCELERATION OF INTENSE ION BEAMS IN MAGNETICALLY INSULATED GAPS†

S. Humphries, Jr., J. R. Freeman, J. Greenly,* G. W. Kuswa, C. W. Mendel, J. W. Poukey and D. W. Woodall**

Sandia Laboratories, Albuquerque, NM 87185

Abstract

Experiments are described pertaining to the development of very high current pulsed linear ion accelerators utilizing electron neutralization. These have application as inertial fusion drivers with intermediate mass ion beams of greatest interest. Progress has been made in a number of areas. A novel magnetically insulated gap using radial magnetic fields has been tested. It provides stable electron cloud confinement over microsecond time scales with no detectable leakage current. The gap can act as an ion injector when used in conjunction with a plasma source. Control of the electron cloud dynamics allows the injector to operate in an enhanced current density mode (10-50 times the Child-Langmuir limit) with high efficiency and with plasma source control of the current flow. Currents up to 20 kA at 100 kV applied voltage resulted when using a light ion flashboard. Carbon beams were produced by extraction from a flowing plasma from a gun array. A 3 kA beam with equal fractions of C^+ and C^{++} was extracted over a microsecond time scale with little proton contamination. The use of active

†This work was supported by the U. S. Department of Energy.

plasma injection into the high intensity magnetically insulated diode had the advantages of ion species control, reduction of gap damage, operation at constant impedance, elimination of plasma closure effects, and a demonstrated ability to control the extracted beam optics. A model is advanced to explain the ion current density enhancement and space charge effects in the gap. Observations were also made of beam propagation and compared to fast neutralization models. Agreement was good, and an upper limit of 0.2 percent was calculated for the imbalance of ion and electron space charge. When using the carbon injector, two-thirds of the beam reached a second magnetically insulated gap where it was post-accelerated. The second gap had an applied voltage in the range 150-200 kV with beam currents typically 2 kA. Observations were made of electrostatic focusing in the post-acceleration gap. These were in good agreement with theory based on the concept of virtual electrodes determined by the neutralizing electron dynamics. The focusing properties could be varied by changing the shape of the regions accessible to electrons.

I. INTRODUCTION

In this paper, we will describe the development of high intensity injectors of protons and intermediate mass ions and the post-acceleration of the resulting beams in a second high voltage gap. The primary motivation for this work was the investigation of the physics of high current pulsed linear ion accelerators for inertial fusion applications.[1,2,3] Ion beams have a number of advantages for use as inertial fusion drivers in comparison to photons and electrons.[4,5,6] Ions are expected to transfer their energy classically to the target. They have favorable energy deposition profiles, and the range can be adjusted by choice of ion species. Beams can be produced with high efficiency and focused to the target without the use of physical lenses. In addition, power multiplication is possible by velocity bunching of the non-relativistic particles. One approach to ion beam fusion is the use of high power, single stage light ion injectors.[7,8,9,10,11,12] These devices, which utilize the high power pulsed voltage technology originally developed for electron beam fusion[13] have shown remarkable progress in the past four years. Focused proton current densities exceeding 100 kA/cm^2 in the MeV range have been produced.[12] This area has also stimulated studies of high current ion beam propagation and neutrslization. There are two major problem areas with respect to the ultimate application of light ion injector technology to fusion reactors. First, because of the limited beam quality obtainable from a single acceleration stage, it may not be possible to focus ballistically the resulting beams to the target with sufficient standoff. Second, the extremely high instantaneous power and energy flux requirements in the injector make high repetition rate and long component lifetime difficult to achieve. One method we are investigating to alleviate these problems is the production of ion beams by multistage acceleration.[1,14]

In a multiple accelertion gap device, electric energy would be converted to beam kinetic energy in a large number of medium power stages. By expanding the conversion process in space and time, the requirements on power and energy flux in a stage would be greatly reduced. In addition, the angular divergence of the injected beam could be lessened by post-acceleration, allowing greater standoff of the final lens from the target. The most familiar example of the multistage ion beam accelerator is the heavy ion fusion approach.[15] The impetus of this program is the development of credible beam production methods using conventional ac elerator technology only, which limits consideration to unneutralized ion beams. In order to achieve the required beam power while remaining within the limits set by unneutralized beam transport, relatively low currents (< 1 kA) of heavy ions at extremely high energies (30 GeV) would have to be used. Heavy ion fusion accelerators would be complex and expensive. In our approach, we hope to use the knowledge gained from light ion injector development on the neutralization of high current ion beams to relax the space charge limits and simplify the accelerator. Parameters typical of a neutralized linear ion accelerator would be intermediate mass ions (i.e., Ne^{+}) at 500 MeV with a beam current of 200/N kA, where N is the number of parallel modules.[2]

It is useful at this point to review briefly the physics of neutralized linear ion accelerators. This will provide a frame of reference to judge the relevance of the experimental results presented in this paper. The major difference from a conventional accelerator is that is is proposed to provide electron neutralization of the beam over the majority of the accelerator length, allowing the transport of higher ion currents. The electrons, having low mass, can rapidly be pulled into the volume of the ion beam over nanosecond time scales. This process continues until the space charge

potential of the beam is depressed to a very low level. In the acceleration gaps, complete neutralization cannot occur since a charge imbalance is needed to obtain a solution to Poisson's Equation. In order to minimize transverse charge effects, the gaps should occupy as small a fraction of the accelerator length as possible. If the gaps are narrow, image charges can also help to reduce space charge effects. The major requirement for successful neutralization in the drift tubes is that electrons must be prevented from escaping into the acceleration gaps. This would cause a large power drain and also prevent the build-up of an effective negative space charge density.

A geometry that is well suited to neutralized ion beam acceleration is shown in Fig. 1.[1] A set of four coils produces a radial magnetic field in the acceleration gap. This field acts to insulate the gaps against electron flow so that high field stress ($\sim$ 300 kV/cm) can be applied over microsecond time scales. Of equal importance, the magnetic flux surfaces prevent electron escape from the drift tubes, allowing effective neutralization. The flow of electrons along field lines bordering the gap can be important in determining the electric field distribution. For instance, the transverse components of the accelerating field pull electrons in along the magnetic field line penetrating the farthest extent of the cathode into the gap. This line then determines an equipotential surface which acts aa a virtual cathode surface.[8] Similar considerations apply to the anode side.[1] If the magnetic fields are shaped as shown in Fig. 1, the accelerating electric field will be similarly shaped to provide strong electrostatic focusing forces for transverse beam confinement. At the high current levels anticipated for the neutralized linear accelerator, acceleration will probably be electrostatic, using pulse forming networks in conjunction with either

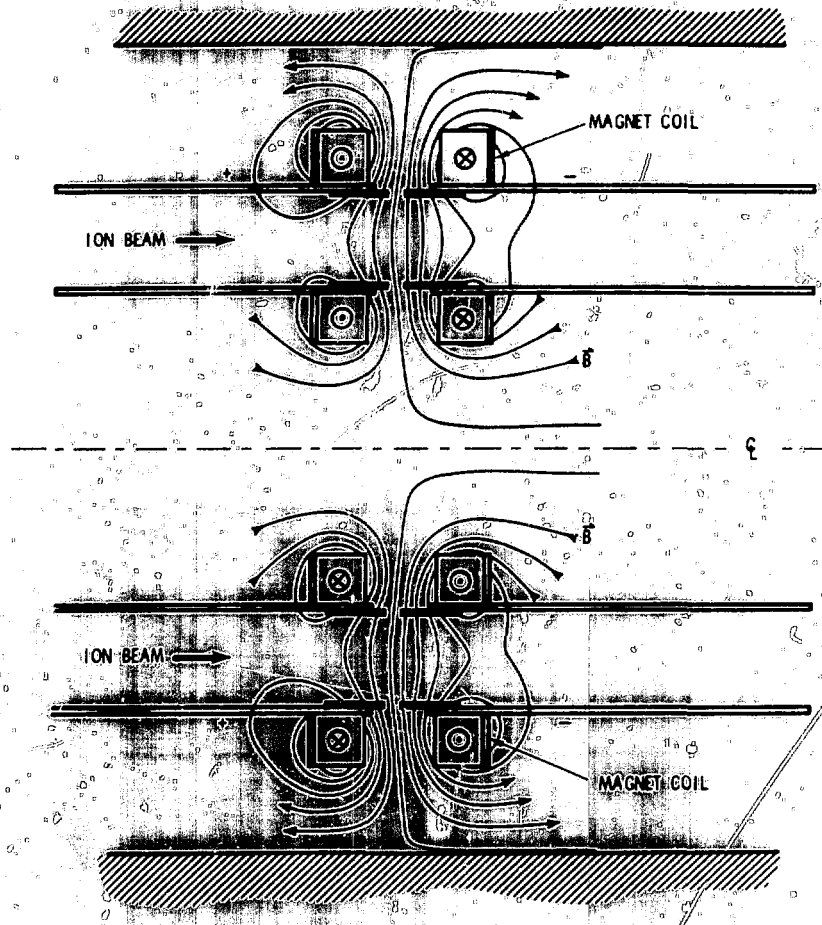

FIGURE 1 *Geometry and calculated field lines for the four coil, magnetically insulated gap.*

inductive coupling[16] or resonant electrostatic drive.[17] For this case, there is no coupling between longitudinal and transverse confinement as in RF accelerators[18] so that the accelerating field can be used for both functions.

There are strong constraints that imply that the geometry of Fig. 1 (and possible related variations[19]) may be the only possible geometry for neutralized ion beam acceleration at high current levels. The magnetic fields are a necesaity, since they allow high field stress to minimize the space charge forces, and they prevent the backflow of neutralizing electrons. The latter function could be performed by thin physical foils covering the drift tubes, but this is obviously impractical for a high duty cycle application. Given that the magnetic fields are unavoidable, there is a choice of two orientations perpendicular to the longitudinal accelerating potential, radial (B_r) or azimuthal (B_θ). Azimuthal fields must be excluded since they would cause discontinuous radial drifts of electrons at the gaps. These drifts would result in electron loss instabilities.[20] Azimuthal fields would also cause ion beam deflections. The only viable choice is a radial magnetic field. Electron drifts in the combination of electric and magnetic field are in the azimuthal direction, and electron orbits can be stable and self-connected. An additional benefit is that ions with paraxial oribits gain no net azimuthal velocity in passing through the fields surrounding a gap. This can easily be shown by invoking conservation of canonical angular momentum. (Calculations of ion orbits in the magnetic fields of Fig. 1 are presented in Appendix I). Whatever its configuration, the neutralized linear ion accelerator opens up a wide range of possibilities for advances in accelerator physics and technology. In contrast to conventional accelerators where only the beam ions themselves must be

considered, the dynamics of both the beam and neutralizing electrons are of equal concern. The addition of a second species creates a wide range of new phenomena for study, including the electron neutralization process itself,[21,22] the transverse confinement and preservation of emittance in highly non-linear focusing systems,[19] and the longitudinal stability of non-relativistic beams in neutralized pulseline driven accelerators.[23]

In the experiments reported in this paper, we were able to obtain information on a number of the aspects of intense ion beam production, neutralization and post-acceleration. We operated a two stage accelerator using an inductively isolated electrostatic drive for the second stage. This apparatus and related equipment will be described in Section II. Section III is devoted to the first stage injector. We produced both proton and carbon ion beams. The carbon ion gun was run with an independent plasma source. With this gun, we were able to demonstrate the ability to control the ion species, current flow and gap impedance, and macroscopic beam optics. Observation of neutralized beam propagation in the drift tubes are presented in Section IV. Results are in agreement with theoretical models; the negative electron space charge balanced the ion space charge to better than 0.2 percent. The post-acceleration of ions in the second gap is treated in Section V; Section VI contains observations of ion focusing by curved virtual electrodes in the second gap. Finally, the implications of the present results on the design of multistage ion accelerators at the kiloampere level are discussed in Section VII.

II. EXPERIMENTAL APPARATUS

A general view of the experiment is shown in Fig. 2. It consisted of an injector gap and a post-acceleration gap. Each gap had its associated pulsed high voltage supply, magnet coils, and magnet supply. The injector

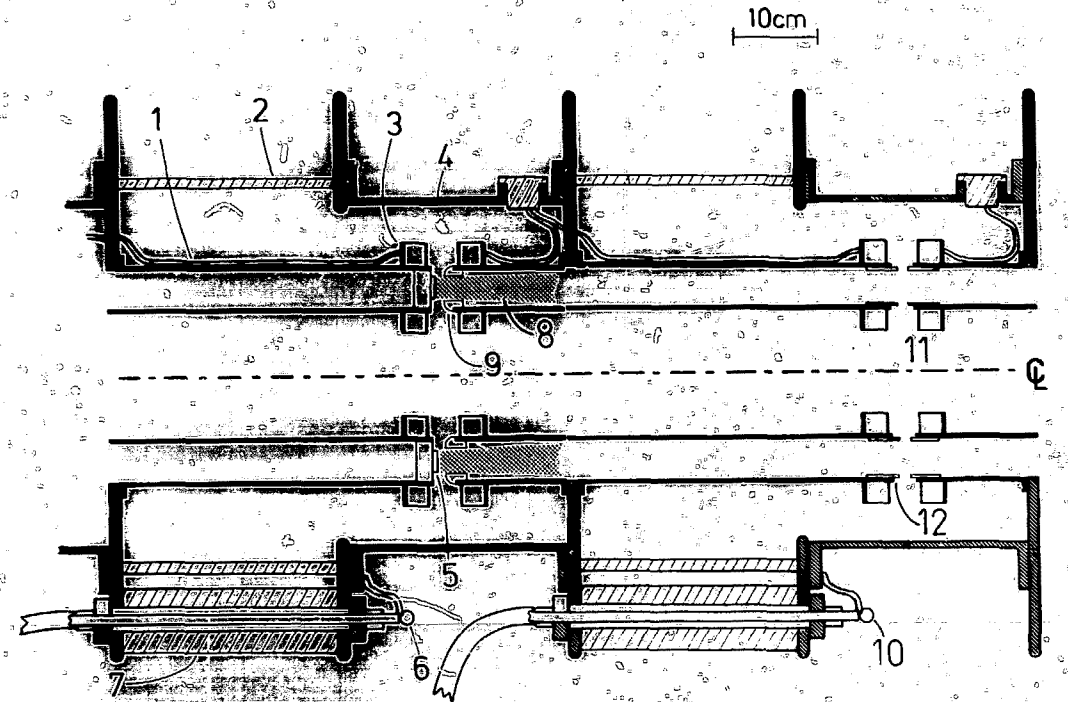

FIGURE 2 Experimental apparatus for two gap acceleration experiment. 1) Magnet power cable. 2) Lucite insulator. 3) Magnetic coil on stainless steel drift tube structure. 4) Aluminum vacuum chamber. 5) Anode plasma flashboard. 6) High voltage feed from Marx generator 1. 7) Oil housing. 8) Emerging proton beam. 9) Injector gap. 10) High voltage feed from Marx generator 2. 11) Post-acceleration gap. 12) Movable gap trimmers.

gap was operated with both proton and carbon inn sources. In the proton mode, the magnetic field geometry was identical to that of Fig. 1: the major difference was the inclusion of a plasma source on the magnetic field separatrix. The second gap also had this magnetic field geometry. The coil construction and placement were carefully performed to provide parallel radial field lines. These defined an acceleration gap with good radial uniformity. Inspection of Fig. 1 shows a general concavity of the field lines upstream. This curvature was purposely introduced by asymmetric coil windings on opposite sides of the gap for focusing experiments (see Section VI). The magnetic field pattern was checked by computer calculations which included effects of conducting boundaries. Details are given Appendix 1.

The four in-vacuum magnetic coils were wound from 120 turns and 60 turns (on the inside and outside respectively) of #16 magnetic wire, and then potted in epoxy. Even though these were exposed to the gap potential and a plasma environment immediately after a shot, there was no problem with breakdowns as long as the coil leads and vacuum feedthroughs were properly potted. The surfaces of the coils were given a thin conducting coat (silver suspended in butyl acetate) to prevent the formation of plasma under high field stress. With the four coils run in series from a 120 μF capacitor bank, the risetime of the magnetic field was 1.25 msec. The drift tube supports were constructed of stainless steel. The accelerator was fired at the peak of the magnetic field to allow full field penetration into the metal supports and to minimize the voltage on the magnet coils during the production of plasma that followed a shot. Typical average radial fields (defined in Appendix I) were 3.2 kG at a bank charge of 5 kV. The coils were tested up to 5 kG.

A. Ion Injectors

The proton injector, shown in Figure 2, used a surface breakdown source[8,24] to produce an anode plasma within the injector gap. This simple device has been used extensively in intense ion beam work. It typically consists of a hydrogenous insulator (polyethylene, lucite, etc.) exposed to the main gap voltage. The insulator is divided into a number of sections by sharp metal dividers, or perforated by a large number of conducting pins. The conductors are connected to anode potential. When the gap voltage is applied, fringing electric fields arise parallel to the insulator surface around the conductors. These can quickly exceed the limit for vacuum surface breakdown (typically 100 kV/cm) producing a plasma at the conductors. The disturbance propagates across the surface until the insulating sheet is covered with plasma. The source of energy for the initiation of the plasma layer is the resistive dissipation of the energy associated with the change in mutual capacitance between the plasma anode and the cathode. In this sense, the flashboard is capacitively ballasted, so that breakdowns occur around all the conductors. Large areas of relatively uniform plasmas can be produced in nanosecond time scales by this method. Ion current densities over 1 kA/cm^2 have been supplied by such devices.[12] In our experiments (with current densities in the range from 10 to 100 A/cm^2) the flashboard could be considered as an unlimited source of ions. The flashboard we used consisted of a 0.6 cm thick annular ring of lucite (11.5 cm O.R., 9.0 cm I.R.) perforated with 500 0.08 cm diameter copper pins. The average spacing between pins was 0.5 cm. The ring was mounted on a conducting carrier which could be moved to adjust the gap spacing. Field shaping electrodes on the cathode side defined a 2.5 cm wide annular slot. Extraction of the ion beam took place entirely through a virtual cathode surface, as shown in Figure 2.

One of the most significant departures of work from past experience was the use of an injector gap that could be used in conjunction with an independent plasma source outside the gap.[25] There were a number of advantages to this approach. The ion species and charge state could be controlled by the plasma gun. (Flashboards have been most useful for light ions, rather than the intermediate mass ions necessary for fusion applications.) Removal of the plasma source from the gap was an improvement in term of repetition rate and lifetime capability of the system. Independent plasma control allowed improvement of the macroscopic beam optics. Finally, we found that the impedance of the injector gap could be controlled by the plasma source. This was not the case with flashboard initiated plasmas, where the gap exhibited a constantly rising ion current.

The geometry of the intermediate mass ion injector is illustrated in Figure 3. An array of six carbon plasma guns was located 20 cm upstream from the injector gap. The magnetic field geometry was changed to allow the plasma to penetrate the gap. As shown in Figure 3, an aluminum field excluding plate was used in combination with the downstream coils. The plasma from the guns expanded through a field free region attaining good uniformity. It then travelled through extraction slots in the field excluder. Approaching the gap, the plasma stagnated at the magnetic field boundary until the gap voltage was initiated. This geometry had the advantages that a parallel annular beam was produced, and a wide variety of pulsed plasma guns could be adapted to the system. The gun array was completely enclosed, allowing the escape of plasma only through the extraction slots. This minimized the possibility that the plasma guns would contribute to breakdowns external to the gap.

With the field excluder geometry, the magnetic field risetime was reduced to 1.0 msec. This gave a calculated penetration depth into the

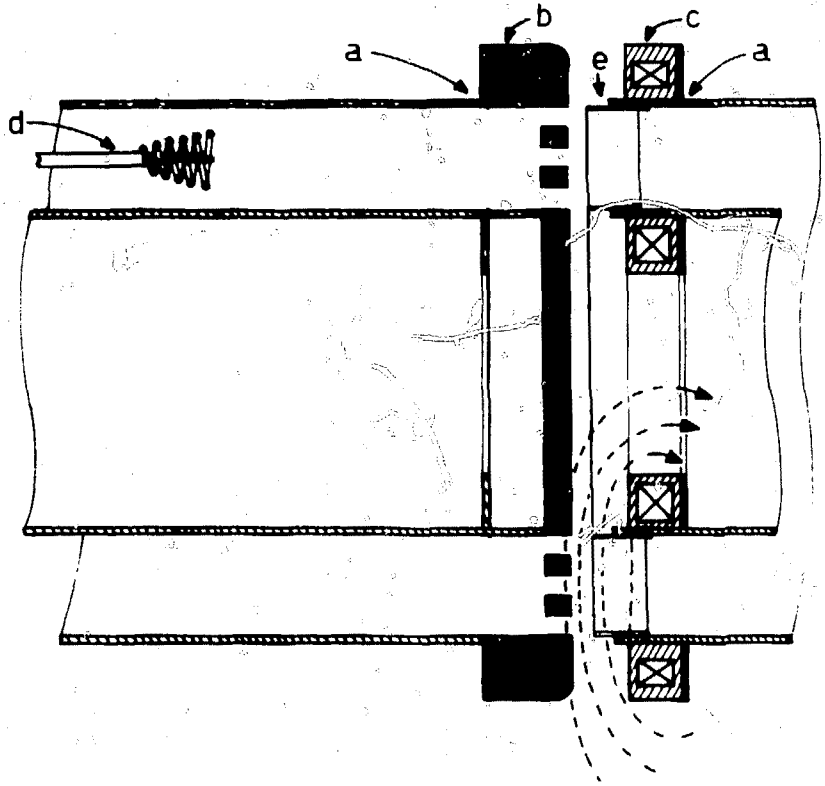

FIGURE 3 Injector geometry for carbon beam production. a) Stainless steel drift tube support structure. b) Aluminum magnetic field excluding structure. c) Magnet coils. d) Plasma gun (One of six used). e) Movable gap trimmer.

aluminum of 0.5 cm at the time of the shot. Two versions of the excluder geometry were used. In the first[26] a single extraction slot of width 2.5 cm was used. Although the operation of the gap from the point of view of ion production was good, the beam propagation was poor. The beam contracted to an annular line focus about 6 cm from the gap. This result supported the concept of virtual electrodes. The magnetic field lines that determined the electron flow bulged into the large slot with about the radius of curvature necessary to account for the focus observed. We corrected this situation by using a field excluder with three smaller slots of width .9 cm with about the same open area (150 cm^2) as the large slot. This excluder is shown in Fig. 3. Another improvement over the initial experiments was the relaxation of electric field stress external to the gap. External breakdowns from the anode drift tube structure to the surrounding vacuum wall at cathode potential were hypothesized to be the main limitation to the pulselength. In order to achieve longer ion extraction pulselengths, the radius of the vacuum chamber wall was increased to reduce the field stress on the wall by 40 percent.

A detailed view of one of the six plasma guns used is shown in Figure 4. These guns initiated a dense carbon plasma by a vacuum surface spark across a Teflon insulator covered with a thin layer of graphite-bearing spray paint. The plasma was accelerated by self-generated magnetic fields. It is shown in Ref. 27 that an efficient magnetically driven engine must have appreciable inductance change in comparison to the inductance of the driving circuit. In addition, it is desirable to transfer most of the energy to the magnetic field before much plasma motion (or inductance change) has occurred. The spiral outer electrode shown in Figure 4 was used to accomplish both requirements. The driving circuit for each gun was

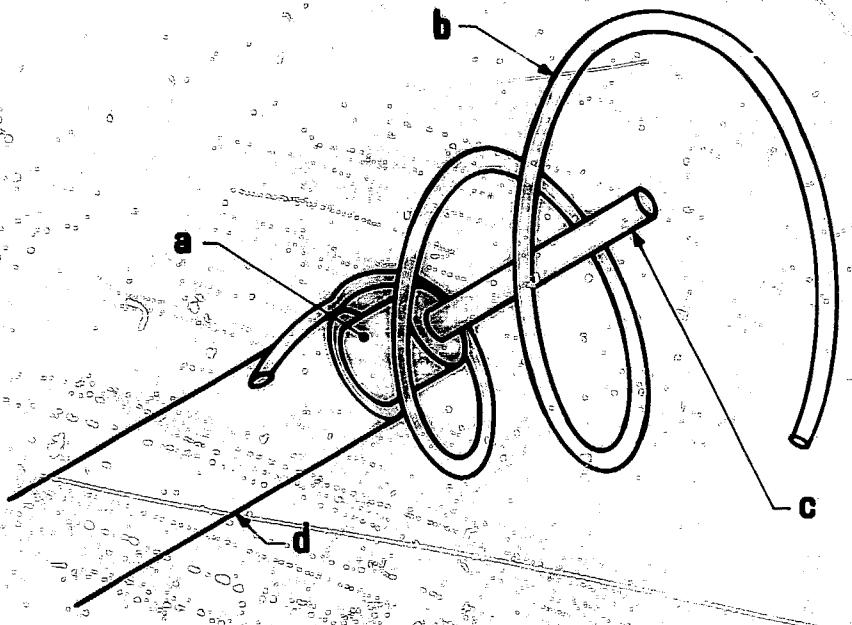

FIGURE 4 Detail of plasma gun. a) Teflon insulator coated with ferrite bar. b) Plasma acceleration coil. c) Central electrode pulsed to positive high voltage (16-22 kV). d) Ground return of rigid coaxial tubing.

a low inductance 0.6 μf capacitor charged to from 16 to 22 kV and switched by a spark gap. Power flowed to each gun through six parallel two meter lengths of Type C (30 Ω) cable. One spark gap fired three guns. The relative timing of plasma guns and injector gap voltage could be varied and showed a jitter of less than ± 100 nsec.

B. Post-Acceleration Gap

The post-acceleration gap (see Fig. 2) was located 30 cm downstream from the injector gap in the optimal configuration. It used the magnetic field geometry of Fig. 1. In this geometry, no field line that intersects the highly stressed regions of the cathode passed near the anode structure. Since there were no direct paths for transport of electrons, electron leakage was very small. The main problem was breakdown external to the gap, along the path indicated in Figure 2. The gap and its surrounding vacuum chamber were originally designed for short pulse operation (50-100 nsec); in this regime it successfully held over 300 kV. In most latter experiments, longer pulses were used and breakdowns were observed at 300 to 600 nsec at about 200 kV. In the long pulse mode, a self-breaking crowbar switch was incorporated into the post-acceleration gap voltage circuit to limit the pulselength to about 200 nsec.

The field lines in the second gap were purposely curved to investigate electrostatic focusing. As described in Section I, this curvature could introduce radial electric field components into the accelerating field to confine the beam to an annular cross section. The magnetic field pattern was fixed, but the effective curvature of the field lines could be changed by varying the position of the gap. This was effected by the use of gap trimmers, thin stainless steel hoops that could be adjusted to protrude into the 2.5 cm wide space between drift tube supports. The post-accelera-

tion gap relied entirely on virtual electrode effects. The full available annulus (5 cm width) was used.

C. Pulsed Voltage Systems

It was necessary to use a variety of pulsed voltage systems. The gap magnet coils were powered by ignitron controlled banks. Typically, a stored energy of 1 kJ per gap was used. Two individually controlled banks were required since the injector gap had a different field risetime than the post-acceleration gap when using the field excluder geometry. With the four coil gap, all coils were run in series. This assured that they all had the same current to achieve the calculated field profiles. The major problem of this type of operation was that the coils on opposite sides of the gap were separated in potential by up to 300 kV. The problem was solved by winding the coaxial magnet supply cable (RG 213) on an isolation inductor. The twelve turn inductor used 25 m of cable and had an inductance of about 40 μH. A number of other cables were run parallel to the magnet cable to supply power and perform diagnostics on the floating parts of the system. For the full two-stage system, two inductor assemblies were used, each having two magnet supply cables for upstream and downstream coils, four diagnostic cables (RG 58), two high voltage cables (RG 59) for charging floating banks to power active boundary electron sources,[28] and one very high voltage cable (Belden 8871) to charge second gap Blumlein lines or directly power the gap. Using the isolation inductors, we were able to perform simultaneously diagnostics on the entire system, even though the stages were at different high voltage potentials. Unfortunately, typical noise levels were on the order of 5-10 volts during the application of the voltages, so measurements were limited to charge collecting probes,[29] voltage and current diagnostics, witness plates and integrated photography.

The injector stage was powered directly from a four stage Marx generator capable of a 200 kV open circuit voltage with a 50 kV charge. The generator stored an energy of 6 kJ at a 40 kV charge and had an inductance of 1 μH. Power was transferred to the air insulated injector through three parallel high voltage cables. These flexible cables allowed opening the system at various points to service plasma guns, adjust gap parameters, or insert diagnostics. The cables passed through oil housings to prevent air breakdown at the separation point of the center conductor from the ground braid. The Marx generator and injector voltage were measured using a resistive voltage divider with a copper sulphate resistor calibrated using a 2000 V pulse. The total generator current was measured by adding signals from three commercial Rogowski loops monitoring each of the cables. There was convenient access to the Marx generator and the air insulated gap, allowing the incorporation of a number of passive circuit elements which could be used to shape the injector voltage pulse. A series resistor of 5 to 15 ohms was added to the Marx generator to minimize damage to the injector from post-pulse breakdowns. A 50 ohm parallel resistance to ground was often included in the Marx generator to eliminate voltage overshoots early in time. These occurred in the proton injector because of its high initial impedance and in the carbon injector following the gap clearing phase (see Section III).

An independent voltage source was used to provide power for the post-acceleration gap. This nine-stage generator had a 450 kV open circuit capability. Two configurations were used for the second gap voltage circuit. In the first, the gap was connected to a 50 ohm, 60 nsec Blumlein line with a floating ground referenced to the potential of the first drift tube. This pulseline was composed of high voltge cables with the center conductor serving as the common connection. The line was charged from a

cable run through an isolation inductor, and was triggered by a gas trigatron switch immersed in an oil housing. The switch was either allowed to self-break with timing controlled by the firing of the Marx generator, or was actively triggered using an inductively isolated trigger line. In the second configuration, the gap was connected directly to the second Marx generator through a 15 ohm series resistor through a cable wound on an isolation inductor. This cable has an electrical length of 120 nsec and a 50 ohm impedance. In this mode, pulselengths were 200 to 300 nsec at 200 kV.

Typically, the following events occurred in a post-acceleration shot with the carbon injector. The second gap magnetic field bank was switched, followed 0.25 msec later by the first gap field bank. In this way the shot was fired at peak field with minimum voltage on both coil sets. At 1.25 msec, the two plasma gun banks were fired simultaneously. The delay for gun turn-on and propagation of the plasma to the injector gap was about 3 to 4 μsec, at which time the first Marx generator was fired. The delay time for the firing of the second Marx generator was influenced by the voltage and current history of the injector and the propagation time of the relevant ion species to the second gap. The delay was typically 400 to 800 nsec.

III. INJECTOR DEVELOPMENT

Initial results on the operation of the injector gap with proton and carbon sources were reported in Ref. 26 and 30. In subsequent work the output characteristics of both sources were considerably improved and a better understanding of factors affecting their operation was obtained. We will first discuss briefly the proton injector, followed by detailed results on the carbon injector. The section concludes with a discussion of the physics of magnetically insulated ion acceleration gaps in the enhanced current density mode.

A. Proton Injector

The capacitively ballasted flashboard that formed the anode plasma in the proton injector was described in Section II. During our experiments, we were able to observe a number of factors that indicated that the plasma production was initiated by capacitive coupling, rather than by electron bombardment as has been suggested.[31] In our magnetically insulated gap, the leakage of electrons across the gap was small. Even if this had not been the case, it was likely that electron leakage would have occurred at the outer radius where $\int B_r dz$ was smallest. It was found, on the contrary, that ion emission took place uniformly with radius and began instantaneously with the application of the voltage. In addition, the response of the plasma anode was very sensitive to the geometry of the conducting pins at the low field stress used (< 200 kV/cm initially). Ion extraction was unreliable if the insulator was thin, if the pins were not sharp, or if the design of the flashboard was greatly modified. For instance, we had little success initiating plasmas with velvet sheets, which show good ion emission at high field stress.[32] After initiation, the plasma was probably maintained or amplified by the flow of diode current.

In its general behavior, the proton injector demonstrated a slow evolution from a high impedance state with Child-Langmuir limited ion flow to a low impedance mode where the current density could exceed the space charge limit by almost two orders of magnitude. This transition took place over time scales on the order of 100's of nanoseconds compared to typical proton transit times of 2 nsec and electron gyroperiods of 0.1 nsec. The early time behavior of the proton injector was investigated using a 70 nsec cable Blumlein line. Two sets of 50 ohm cable were used, to give a total impedance of 50 ohms for the generator. Typical experimental traces are

illustrated in Figure 5. The lines were charged in a microsecond, and then the pulse was initiated by an actively fired trigatron switch. A flat voltage pulse exceeding 200 kV was typically obtained; the late time negative overshoot in Figure 5(b) was caused by the charging inductor in parallel with the gap. The total current was low, even though the full 300 cm^2 of available anode area was used. The small ion current densities were comparable to the space charge limited prediction with some correction for electron effects, since the gap was not run very much above the critical insulating field.[33,34] For comparison, the Child-Langmuir prediction for monopolar proton flow at 240 kV with a 0.7 cm physical gap is 12 A/cm^2. The three charge collecting probes located 2.5 cm downstream from the virtual cathode at different azimuthal positions showed non-uniform ion extraction. This was reproducible and corresponded to inaccuracies in gap alignment.

A downstream time-of-flight probe (Figure 5(g)) gave an excellent proton signal. Because of the flat voltage pulse, there was little velocity dispersion and the bunch was well confined. The delay time was characteristic of protons, and there was no indication of heavier ion species. The general behavior of the proton injector at early times was in good agreement with previous experiments using short pulse, high impedance magnetically insulated ion diodes.[8,24] The ion extraction appeared to be governed by classical space charge flow considerations. Unfortunately, the resulting beams had poor divergence properties. Strong transverse space charge forces acted on the bare beam crossing the gap. Typically, the beams exhibited radial half angles of divergence greater than 7°. We made unsuccessful attempts to correct the radial spreading by introducing a concavity into the plasma anode. In these tests, plasma was produced preferentially at

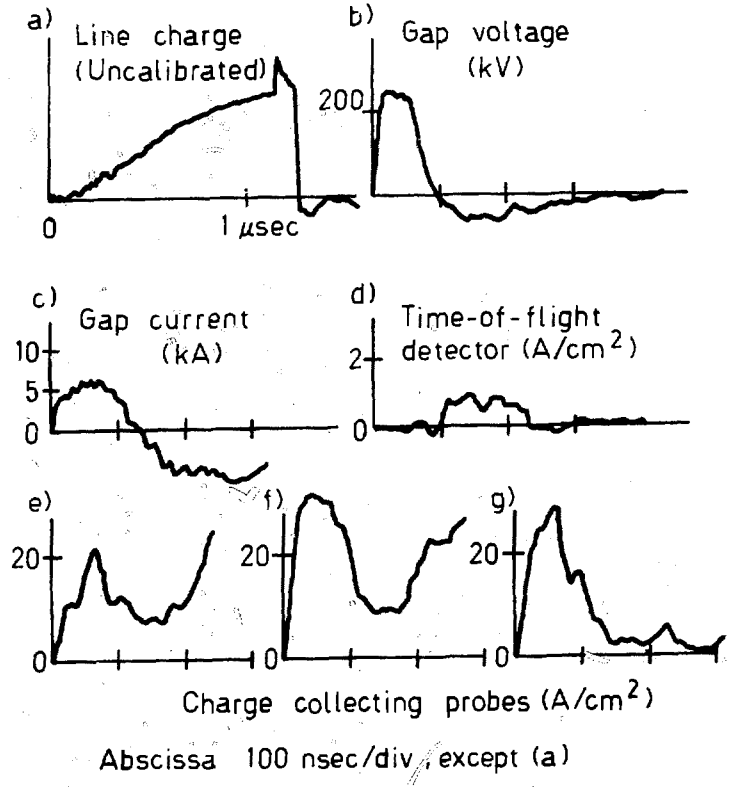

FIGURE 5 Experimental traces for proton injector using flashboard plasma source and 60 nsec Blumlein lines. a) Line charge voltage. b) Gap voltage. c) Gap current. d), e), and f) Signals from charge collecting probes located 2.5 cm downstream on 10 cm radius, at different azimuthal positions. g) Signal from a charge collecting probe 60 cm downstream from gap.

the inner and outer radii of the flashboard where the field stress was the highest. The two resulting beams showed no improvemnt in parallelism. In addition to the macroscopic radial spreading, the beam also showed poor microscopic divergence due to the coarseness of the plasma anode. Damage plates indicated that at early times ion extration was most intense near the initiating pins, probably a symptom of the low electrical field stress used. The combination of low total current and poor beam optics gave very small currents at the location of the second gap which precluded significant post-acceleration experiments.

Many of the problems of the proton injector were alleviated by extending the voltage pulse to longer times. The injector was connected directly to a Marx generator. Experimental traces for operation of the proton injector in the long pulse mode are shown in Figure 6 (a) and (b). In the first case, the injector Marx generator was charged to 50 kV and the average applied radial field was 3.8 kG; in the second, the charge was 60 kV with a 2.5 kG average field. In both cases, the ion current began immediately (as shown by the probe traces). The gap impedance was intially high, reflecting the space charge limited ion extraction. Because of peaking circuit effects, the voltage initally rose to a level higher than the Marx generator open circuit voltage. The extracted ion current density traces shown were obtained with two multiaperture biased charge collectors located 2.5 cm downstream from the gap. These probes had seven apertures distributed radially to give an average of the ion current density. Early in time, the probe signals followed the voltage dependence through the $V^{1.5}$ power scaling characteristic of space charge flow and showed azimuthal non-uniformity. Although the injector began in a manner typical of short pulse devices, after a few hundred nanoseconds it underwent dramatic changes in its

FIGURE 6 Experimental traces for proton injector using flashboard plasma source and direct connection to Marx generator. Left: Voltage and corrected current. Right: Current density at two locations, averaged in radius by multiaperture probe, 2.5 cm downstream from gap.

a) Marx generator charge, 50 kV; applied field, 3.8 kG.

b) Marx generator charge, 60 kV; applied field, 2.5 kG.

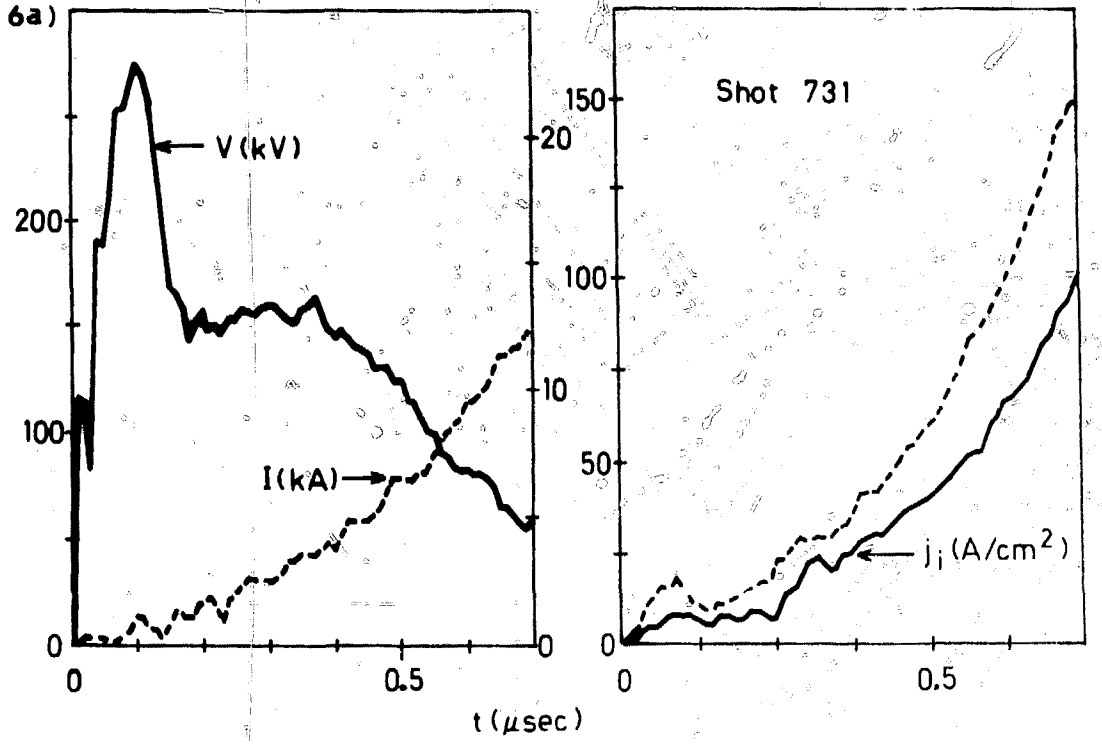
6a)
V(kV)
I(kA)
200
100
0
20
10
0
0
0.5
t(μsec)
Shot 731
150
100
50
0
j_i(A/cm^2)
0
0.5

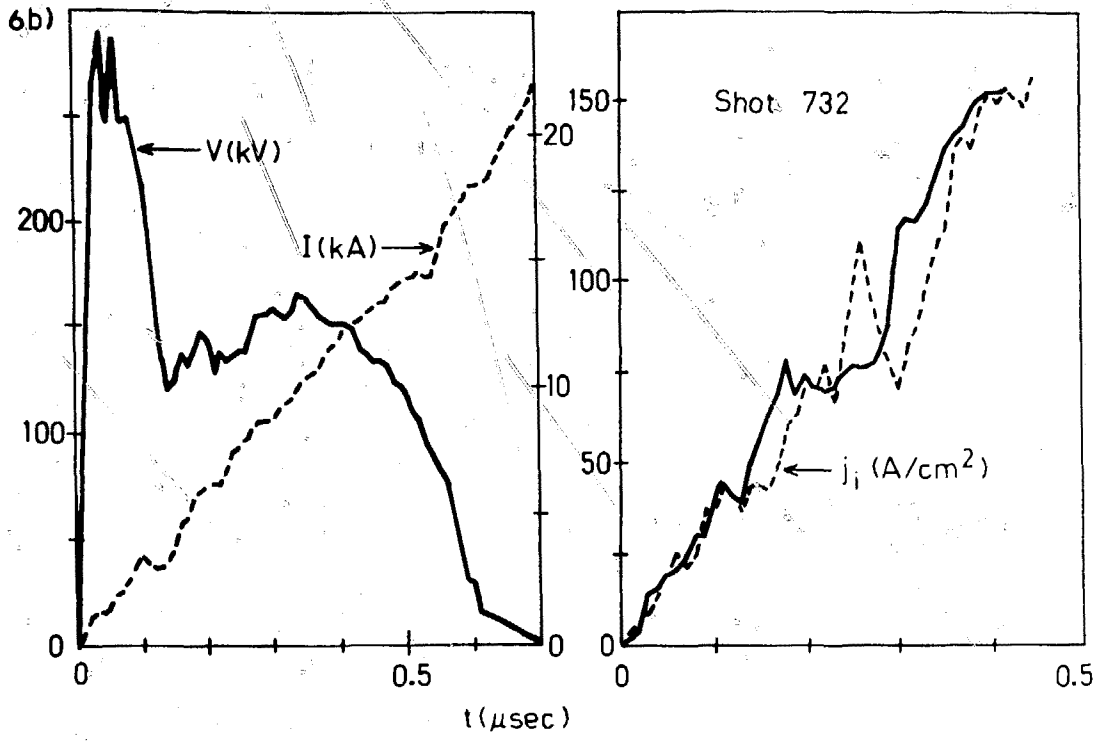
6b)
V(kV)
I(kA)
200
100
0
20
10
0
0
0.5
t(μsec)
Shot 732
150
100
50
0
j_i (A/cm^2)
0
0.5

operating mode. That is, while the voltage decreased, both the total gap current and the ion current steadily increased. This process continued until the ion current extracted from the gap exceeded the capability of the voltage generator and the gap voltage was pulled down. The rate at which the gap evolved toward this mode was sensitive to the applied magnetic field, as can be seen by comparing the current and probe traces for the two shots. The ion extraction efficiency appeared to be very good; the probe signals followed the current monitor closely and had a magnitude close to the the total current divided by the anode area of 150 cm^2. The beam emission was observed to compress radially with time until the output was localized to a narrow band centered about the average gap radius. The strong variations in probe signals at late times are due to the radial changes in emission as viewed by the discrete number of apertures. Neglecting these variations, the probe signals were observed to follow each other closely. One of the most distinctive characteristics of late time behavior was excellent azimuthal extraction uniformity when averaged in radius.

The shot of Figure 6(b) represents the best parameters obtained to date with the 1μH Marx generator. The total pulselength was 630 nsec. The current at 540 nsec was 25 kA; the total number of particles extracted during the useful pulselength was 4×10^{16}. The maximum voltage observed on the intial overshoot was 240 kV, and the average voltage during the pulse was about 125 kV. The extracted ion beam energy was 800 joules. The enhancement of ion current above the Child-Langmuir prediction at late times was very high. At 400 nsec, the charge collecting probes measured an average radial current density of 130 A/cm^2 with a gap voltage of 110 kV. The predicted space charge limited flux for protons is about 4 A/cm^2, implying an enhancement factor of 35.

Even though the initial ion emission was fairly uniform in radius, ultimately most of the extracted flux was centered about the average radius of the annular gap (10 cm) where the magnetic field lines bulged closest to the anode. This was indicated by single aperture charge collecting probes which measured the local ion current density at the 10 cm radius. These probes typically showed signals more than a factor of two in excess of the averaging probes. The extraction of ions in this situation was a strong indication of the existence of a virtual cathode. The bulk of the ion flux was well separated from the physical electrodes which defined a 2.5 cm wide slot (see Figure 2). This was favorable phenomenon from the point of view of performing the experiment. Cathode electrodes composed of thin coats of silver paint over lucite were used for hundreds of shots without damage. A reproduction of the markings on a typical witness plate located 2.5 cm downstream from the virtual cathode is shown in Figure 7. Note that the width of the damage pattern was less than half the width of the plasma anode; also, the ion emission was centered on the average radius only on an average basis, with radial excursions about the mean that varied with azimuth. These variations in emission radius were preserved over the length of a shot at late times and were reproducible from shot to shot. The witness plate shown in Figure 7 had a number of 0.6 cm diameter circular apertures which allowed a portion of the beam to be projected on another witness plate 5 cm downstream. A reproduction of this plate is shown below the first on the same scale. Note that downstream damage occurred behind only those holes overlapped by the main damage pattern. The damage spots were directly behind the holes and were well localized. The width of the patterns implied about a 3° boundary half angle divergence.[35] Note that the damage patterns were rotated clockwise with respect to the apertures. The

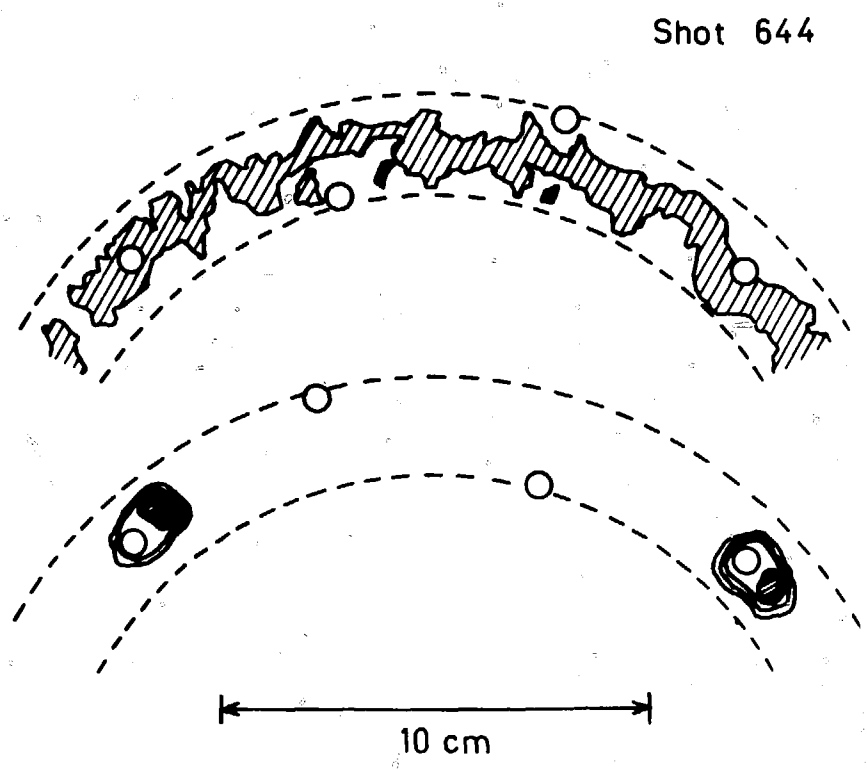

FIGURE 7 Reproduction of witness plates exposed to output from proton injector. Top: Plate located 2.5 cm downstream from gap. Dotted lines show inner and outer radii of flashboard. Circles are apertures in plate. Bottom: Second witness plate, 5 cm downstream from first, drawn to same scale. Inner and outer flashboard radii are shown, as well as projections of first plate apertures.

main damage spots agree in magnitude and direction with the predictions of Appendix I for protons. In this case, the average radial field was 3.2 kG and the average proton energy was about 100 kV, so the rotation of the beam between the two positions is predicted to be 0.9 cm. The damage near the aperture was probably caused by heavier ion species. The predicted deflection for C^+ is 2.5 mm.

Attempts were made to determine the ion species content of the extracted beam. Measurements at Sandia Laboratories[36] and Cornell University[37] using similar flashboards showed that the extracted beams consisted of about 50 to 80 percent protons. We performed a number of tests and ascertained that there was a significant fraction of carbon-like ions, but were not able to make a quantitative determination. Nonetheless, these data are interesting when compared with the same measurements done for the carbon injector, which showed a complete absence of protons. A Thompson parabola ion mass spectrometer gave a qualltative indication of ion species present. There was a strong proton line as well as lines near the expected position of C^+. These data are presented in Section V. A magnetic spectrometer was also used. This consisted of a permanent magnetic field perpendicular to the beam direction with twelve channels. The channel detectors were charge collectors monitored by high input impedance operational amplifiers. In typical operation with a thin slit, the first channel viewed ions with small deflection (i.e., carbon ions in the range of 100 keV) and the second channel viewed protons in the energy range 60 to 90 kV (or C^+ from 5 to 7.5 keV). Because of the high noise level with our system, it was not possible to use the amplifiers, since the spectrometer, amplifiers, and associated power supplies had to be floated at the high negative extraction potential. Instead, the collecting plates were used directly as biased

charge collectors driving a 50 ohm load. In order to do this, a large aperture was used with considerable loss in resolution. Shown in Figure 8(a) are time resolved outputs from Channels 1 and 2, which are comparable in magnitude. The main point to note is that there was definitely a light ion signal present. Measurements were also made using time-of-flight charge collecting detectors a meter from the injector. Typical oscillographs are shown in Figure 9 along with predictions of the relative downstream probe signals for p^+ and C^+ based on analysis of the associated voltage and current waveforms. These signals imply that over 50 percent of the beam consisted of carbon-like ions. This can be misleading since there were processes associated with the beam transport that may have reduced the amount of protons. In order to have beam neutralization, a certain amount of the beam head had to be lost to supply secondary electrons from wall collisions (see Section IV). This would reduce the level of protons since they had a higher velocity than the carbon-like ions. Also, the effects of passing the downstream coils and errors in locating the anode exactly on the magnetic field separatrix could have induced stronger deflections on the proton orbits (see Appendix I).

B. Carbon Plasma Guns

Proceeding to the carbon ion injector, we will first discuss measurements of the characteristics of the plasma guns. These simple and vesatile devices have been used extensively in experiments at Sandia Laboratories, particularly in providing plasma prefill for low impedance electron diodes. Previous spectroscopic measurements[38] showed that the plasma consisted roughly of equal parts of C^+ and C^{++}. These moved in a sharp front at about 7×10^6 cm/sec. Low density neutral carbon with a velocity of 0.5×10^6 arrived much later; neutral hydrogen was undetectable. At about

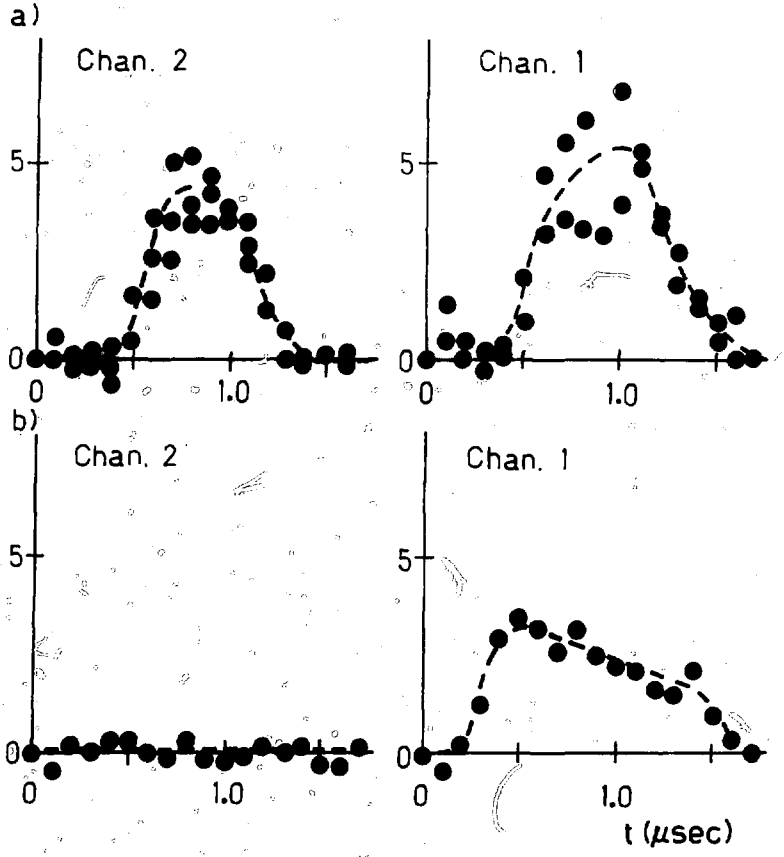

FIGURE 8 - Signals from magnetic spectrometer. Channel 1 indicates ions with high mass; Channel 2 is optimized for protons in the 100 keV range. a) Proton injector with flashboard anode plasma. b) Carbon injector with plasma gun array.

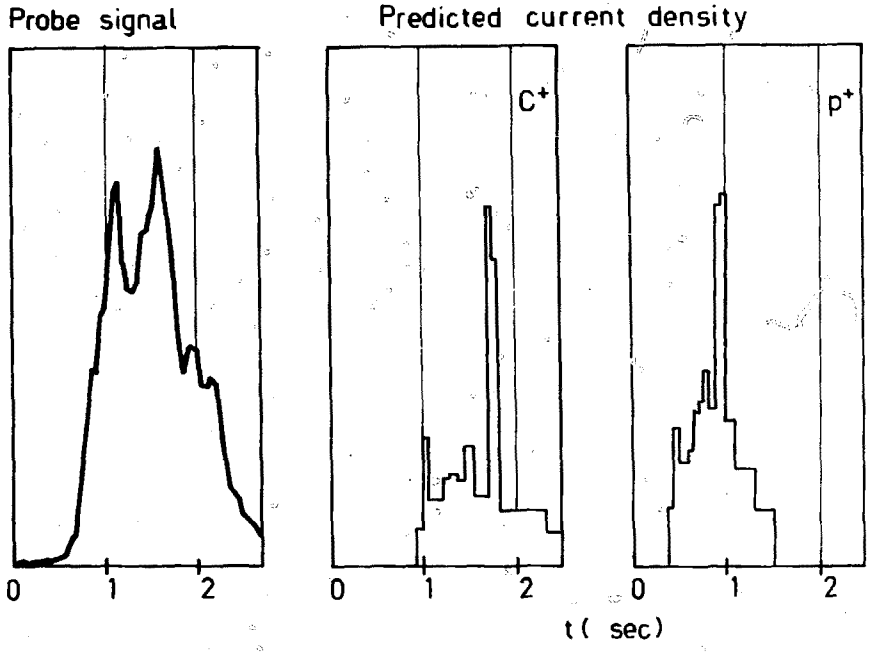

FIGURE 9 Time-of-flight data for proton injector with flashboard anode plasma source. a) Relative signal from probe 1 m downstream from injector. b) Predicted probe signals from measured voltage and current of injector. Predictions for C^+ and p^+ are for equal currents of each species; not to scale with trace of (a).

20 cm from the end of the gun the electron density during the microsecond pulse was found to be about 10^{13} cm^{-3} from microwave interferometry. We built a test stand to make further measurements on the available ion flux from the guns. It was a 30 cm diameter glass vessel, 50 cm in length, with provision for mounting a variety of diagnostics and plasma guns on the end flanges. A 1 m vacuum extension allowed time-of-flight studies. The main quantity of interest from the point of view of ion injection was the ion flux produced by the guns. This was measured with temporal and spatial resolution by the use of standard biased charge collecting probes. These consisted of a defining aperture 1 mm in diameter with a negatively biased collector 3 mm behind. Plasma bulged through the aperture; a -30 V bias turned the electrons so that only the forward directed ions were collected. Secondary electron emission processes were small at the low plasma ion energy. Because of the low ion energy and bias voltage, the probes were found to be sensitive to the cleanliness of the collector surface. Best reproducibility was obtained by selecting a probe with a good response and moving it spatially on a shot-to-shot basis. A typical probe signal ia shwon in Figure 10(a). A single gun was used, with the probe at a distance of 20 cm, corresponding to the spacing between the gun array and the anode in the actual experiemnt. The plasma pulse duration was about 2 μsec. The plasma flux at 20 cm peaked about 3.0 μsec after firing the gun, giving an average drift velocity of 6.7 cm/μsec. This corresponded to an energy of 280 eV for carbon. The peak current density on axis was about 10 A/cm^2. Combining this with the average flow velocity yields an ion density of $n_i = 9 \times 10^{12}$ cm^{-3}, in agreement with the interferometric electron density measurements. This trace was taken with a plasma gun bank charge of 18 kV, a typical value used in experiments.

The spatially resolved peak ion flux is shown in Figure 10(b) at two distances from the gun. The half width of 9 cm at 20 cm distance is consistent with the 30° plasma divergence observed on time-integrated photographs of the gun in operation. This angle corresponded to the cone angle of the helical outer conductor winding (see Figure 4). The small scatter of points in Figure 10(b) is indicative of the good shot-to-shot reproducibility of the guns. Following recoating of the graphite and system pumpdown, two shots were needed to clear the guns of solvents and absorbed gases, after which they could be fired for 20 to 30 shots with little change in output. The single gun flux density spatial variation was used to calculate the total flux density of the six gun array at the location of the anode slots. The results of this calculation for the 10 cm injector radius are shown in Figure 10(c). With an 18 kV bank charge and a 3 μsec delay, the average current density of ions was predicted to 23 A/cm^2 with a 7 percent variation with azimuth.

Measurements were made of the variation of plasma parameters with the charging voltage of the plama gun bank. Results are shown in Figure 10(d). The peak plasma flux (measured by a charge collecting probe at 50 cm distance) scaled approximately as V_b^2, as indicated by the least squares power law fit to the data. The delay from firing the gun to the detection of the peak plasma flux is also plotted. This scaled approximately as $V_b^{-0.8}$. Some measurements were made of the plasma flow properties in situ using the full gun array. Charge collecting probes and Langmuir probes were used at the exits of the injector anode slots. With no applied field, traces were similar to those of Figure 10(a). With a magnetic field present, the arrival of the plasma was delayed, typically by about 1 μsec. This was caused by the penetration of the field into the field excluder, which had a

FIGURE 10 Plasma gun test stand measurements. a) Oscillograph of ion flux versus time. Probe at 6.4 cm radius, 20 cm from gun. Ordinate: 2 A/cm^2/div. Abscissa: 1 μsec/div. b) Spatial dependence of ion flux from one gun, 18 kV bank charge. Time is measured from initiation of gun voltage. c) Predicted spatial variation of ion flux from six gun array using spatial distribution indicated by dashed line in (b). 10 cm system radius. 20 cm from gun array. d) Variation of gun parameters with bank charge.

10a)

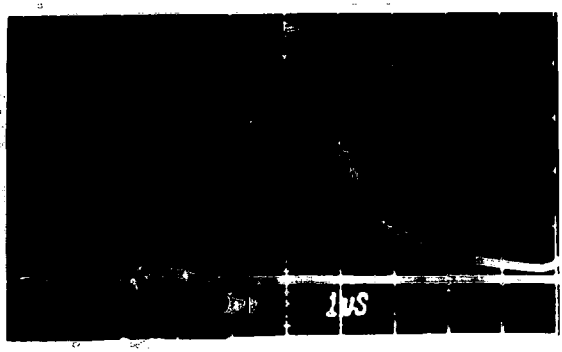

10b)

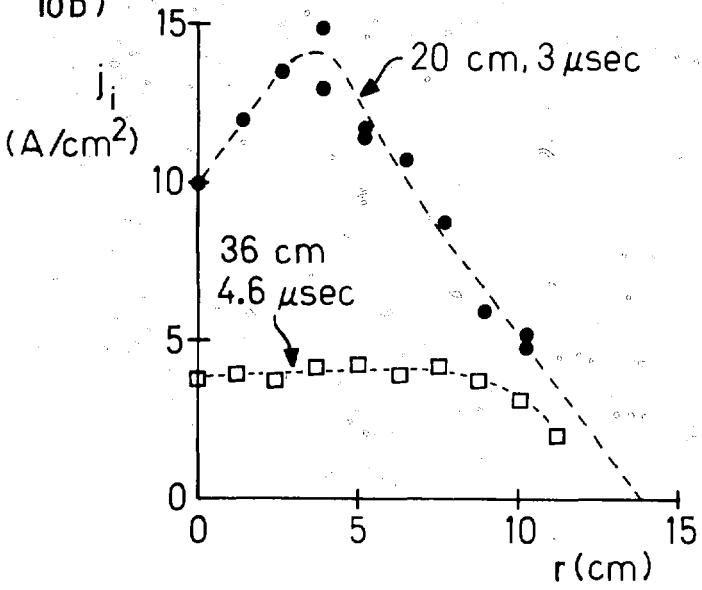

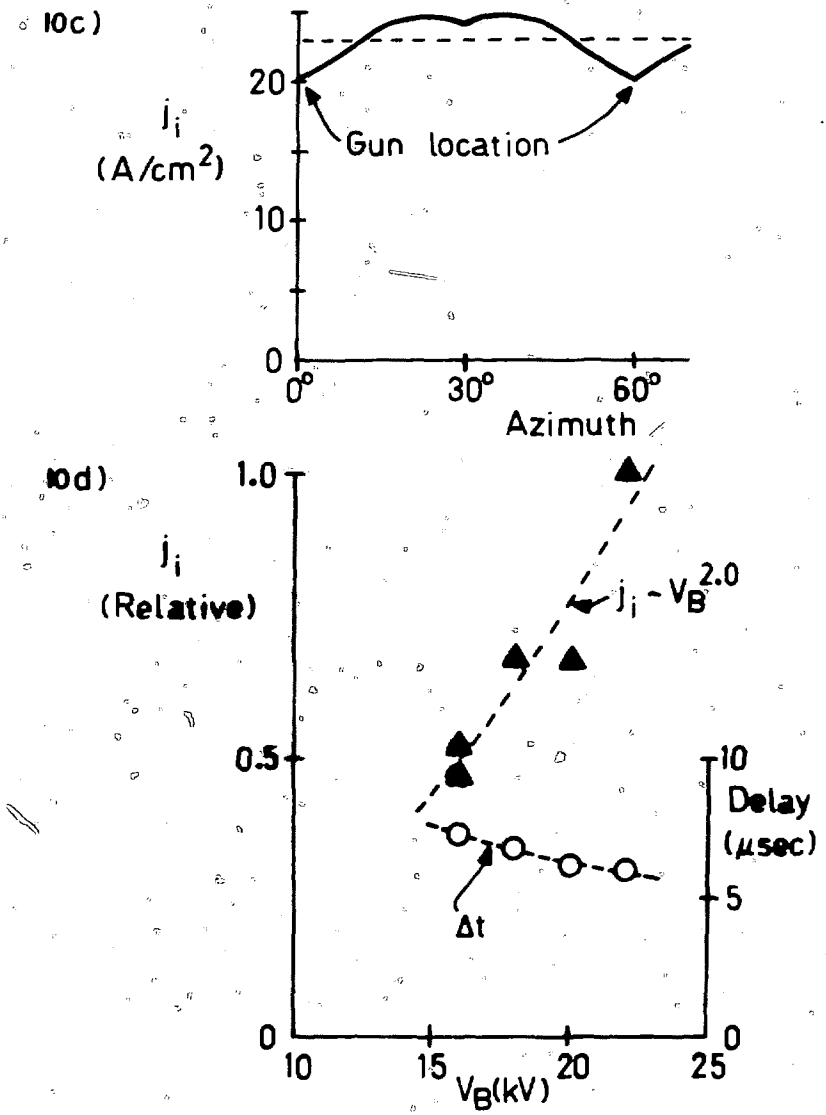
(c)
20
10
0
j_i
(A/cm^2)
Gun location
0°
30°
60°
Azimuth
(d)
1.0
0.5
0
j_i
(Relative)
$j_i \sim V_B^{2.0}$
10
Delay
(μsec)
5
0
Δt
10
15
20
25
V_B(kV)

skin depth of around 0.5 cm for the 1 μsec magnetic field risetime. Probe measurements showed that the plasma stagnated upon reaching the magnetic field barrier, but untimately could diffuse across the field lines. Thus, depending on the delay between plasma gun initiation and the injector voltage pulse, the injector gap could have a plasma prefill.

C. Injector Gap

Following plasma gun measurements, experiments were carried out on the magnetic insulation properties of the injector gap with field excluder. The gap voltage was applied without firing the plasma guns. It was found that the insulation properties of the gap were even better than the full four coil gap. This was probably because the field excluder acted to correct small errors in the field from the construction and alignment of the magnet coils. Typical results are shown in Figure 11. Plotted are the gap voltage, the total measured generator current, and the predicted generator current from circuit losses not associated with the magnetic diode. (These came about because of a 30 ohm parallel resistor in the Marx generator and the 40 μH diagnostic isolation inductor). The open circuit Marx generator voltage was 120 kV and the applied field was 3.2 kG with a 0.7 cm physical gap. As can be seen, the total voltage pulse approached 2 μsec. For the first 1.6 μsec, the was no detectable leakage current. We feel that the absence of leakage current is due to the stable confinement of the cathode electron cloud rather than the delayed emission of cathode electrons. The cathode gap trimmer was stainless steel shim stock of 0.03 cm width, which would be subjected to greater than a MV/cm field stress in the absence of virtual cathode formation. At late times, there was an increasing leakage current that ultimately lead to a breakdown. Integrated photographs and damage inspections showed the breakdown occurred

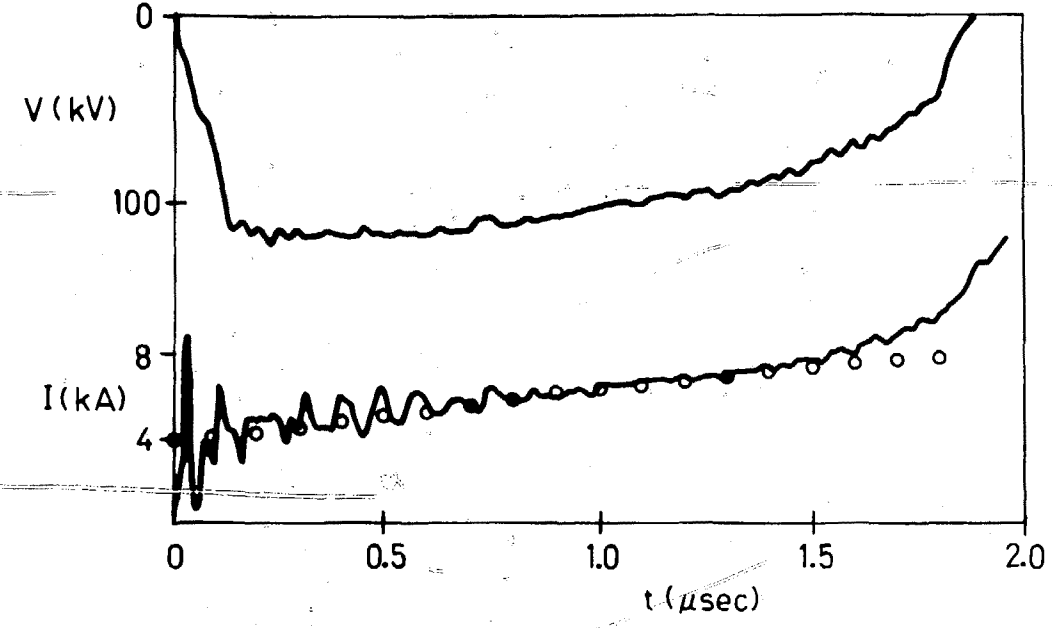

FIGURE 11 **Magnetic insulation tests.** Three slot carbon ion injector with no injected plasma. Top: Gap voltage. Bottom: Solid line is measured total generator current. Circles represent predicted current lost to 30 ohm damping resistor and 40 μH diagnostic inductor. Difference between measured and predicted values represents leakage currents in system.

in a non-magnetically insulated part of the system a full 20 cm upstream for the gap.

Full system shots (with carbon plasma injection, magnetic insulation, and applied gap voltage) were taken under a wide variety of circumstance. We will first discuss a typical shot, and then consider how the injector was influenced by changes in parameters such as gap voltage, plasma bank charge, relative delay, and so forth. The reductions of experimental traces in Figure 12 are from an average shot. The injector Marx generator charge was 45 kV, the applied radial field was 2.5 kG, and the plasma gun bank charge was 18 kV. Using the 0.7 cm physical spacing of the gap, the magnetic field $\overline{B}_r$ was 70 percent above the critical insulating field. The injector voltage pulse was delayed 3.2 μsec from the firing of the plasma gun, so that the plasma had already reached the magnetic stagnation point at $t = 0$. Initially, the injector gap proceeded through a low impedance phase, associated with clearing the plasma prefill. After about 0.1 μsec, the impedance rapidly rose by about a factor of 60, and the gap settled into an equilibrium mode until about 0.8 μsec. The voltage drop during this time was accountable in terms of the isolation inductor and damping circuit elements in the Marx generator. After 0.8 μsec, the corrected current (the total current minus the current flowing to ground through passive circuit elements) rose rapidly, and a breakdown external to the gap brought the voltage to zero at 1.2 μsec. Biased charge collecting probe signals from this shot are also shown. The probes were located 7.6 cm downstream and were 180° apart in azimuth. One probe was located at the average radius of the inside slot of the three slot injector, while the other viewed the outside slot. Because of the good beam quality, the current density measured by these probes was close to that at the virtual extraction cathode.

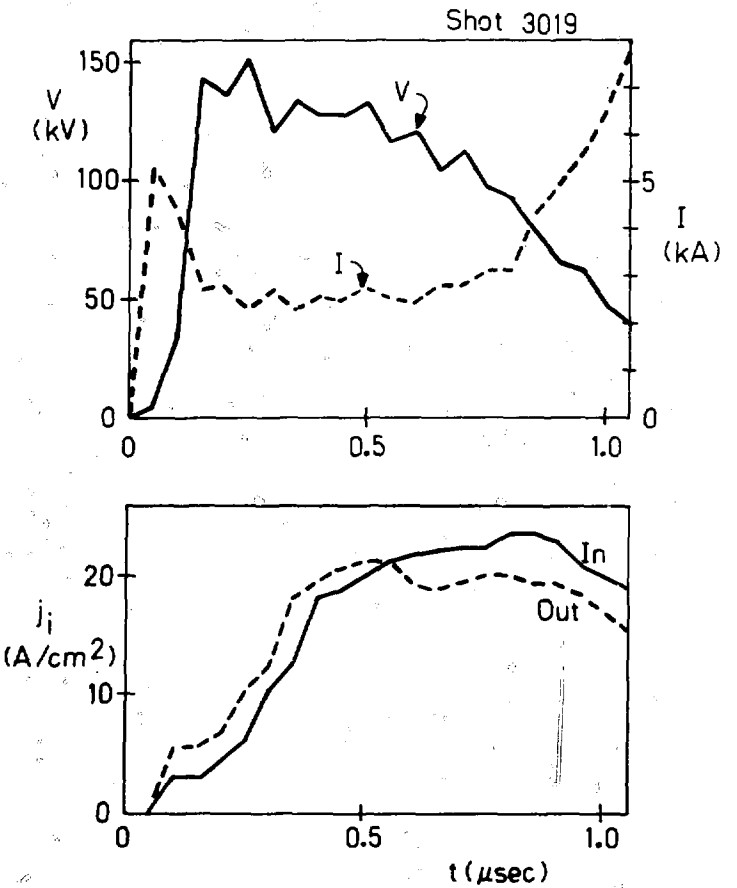

FIGURE 12 Shot with carbon ion injector. Marx generator charge: 45 kV, applied magnetic field: 2.5 kG, plasma bank charge: 18 kV, delay between firing plasma guns and injector gap: 3.2 μsec. Top shows measured gap voltage and current with external circuit losses removed. Bottom shows charge collecting probe signals from probes 7.6 cm downstream.

Initially, there was a delay of 50 nsec to the detection of ion current resulting from the transit time of the low energy ions to the detectors. Early in time, during the gap clearing phase, the probe response was low. This was probably due to inhibited propagation of the dense, low energy ion beam through the region of radial magnetic flux. After the clearing phase, the probe signals reached an equilibrium level of about 21 A/cm^2. This equilibrium behavior was in marked contrast to that of probes viewing the proton injector with flashboard plasma source, where the ion current density climbed continuously. The probe traces of Figure 12 actually show a decreasing ion current after 0.8 μsec. Another marked difference is that the probes measured good radial uniformity of emission from the three injection slots, whereas the proton injector had emission strongly peaked on the average radius. In both injectors, average azimuthal uniformity was good. Although the carbon injector did not exhibit radial variations, there were some differences in probe response with radius. The outer channel always approached equilibrium faster, as shown in Figure 12. Upon reaching the equilibrium phase, though, there were no significant differences in probe response. The equilibrium probe signals were in good agreement with the gap current measurement to the limit of experimental accuracy. (Dividing the 2.6 kA corrected current by the 150 cm^2 area of the extraction slots gives a value of 17 A/cm^2.) The most interesting feature of the injector gap current density measurement is the fact that the measured value is very close to the measured anode plasma flux (23 A/cm^2). This figure should be compared to the Child-Langmuir prediction for the physical gap and applied voltage, which is only 1.2 A/cm^2 for C^+ and 1.7 A/cm^2 for C^{++}.

A number of tests were performed to determine whether the equilibrium injector current was controlled by the carbon plasma flux entering the anode slots. Figure 13 shows an example of experimental traces where the Marx charge was varied with the plasma bank charge, relative timing, and applied magnetic field maintained constant. Note that in proceeding from a charge of 30 kV to 45 kV, the corrected current (at 0.3 μsec) increased from 2.4 to 3.3 kA, a 40 percent difference. Child-Langmuir scaling implies that the current should have increased by a factor of 2. Regarding the probe signals, there was no significant difference in the extracted ion current density between the two shots. In this shot, the probes viewed the middle and outside slot. Note that again the outside probe had the fastest risetime, and that in equilibrium there was good agreement between the two probes. The lower current densities compared to those of Figure 12 resulted from the fact that the plasma gun bank was charged to only 16 kV in this case.

In was difficult to perform tests of current density variation with the charge of the plasma bank because of interferring effects. At high bank charge, the plasma arrived at the gap earlier and often exacerbated external breakdowns. Nonetheless, some qualitative features of shots with different bank charge are noteworthy. A case with high bank charge (22 kV with a 2.9 μsec delay) is shown in Figure 14(a). The current density measured by the probes began almost instantaneously and rapidly built up to a high level, paticularly in the outer slot. Unfortunately, the gap was shorted before equilibrium was reached. It is interesting that even though the gap voltage was almost zero at late times, the ion current measured by the probes continued. This was not due to probe shorting, but rather to the fact that the plasma continued to enter the gap. Late time low energy ion signals disappeared when the probes were moved farther back from the injector

FIGURE 13 Carbon injector shots with Marx generator charge varied. Shown are gap voltage, corrected current, and downstream current density from probes viewing middle and outside slots at different azimuths, 7.6 cm from injector. a) Marx generator charge, 30 kV. b) Marx generator charge, 45 kV.

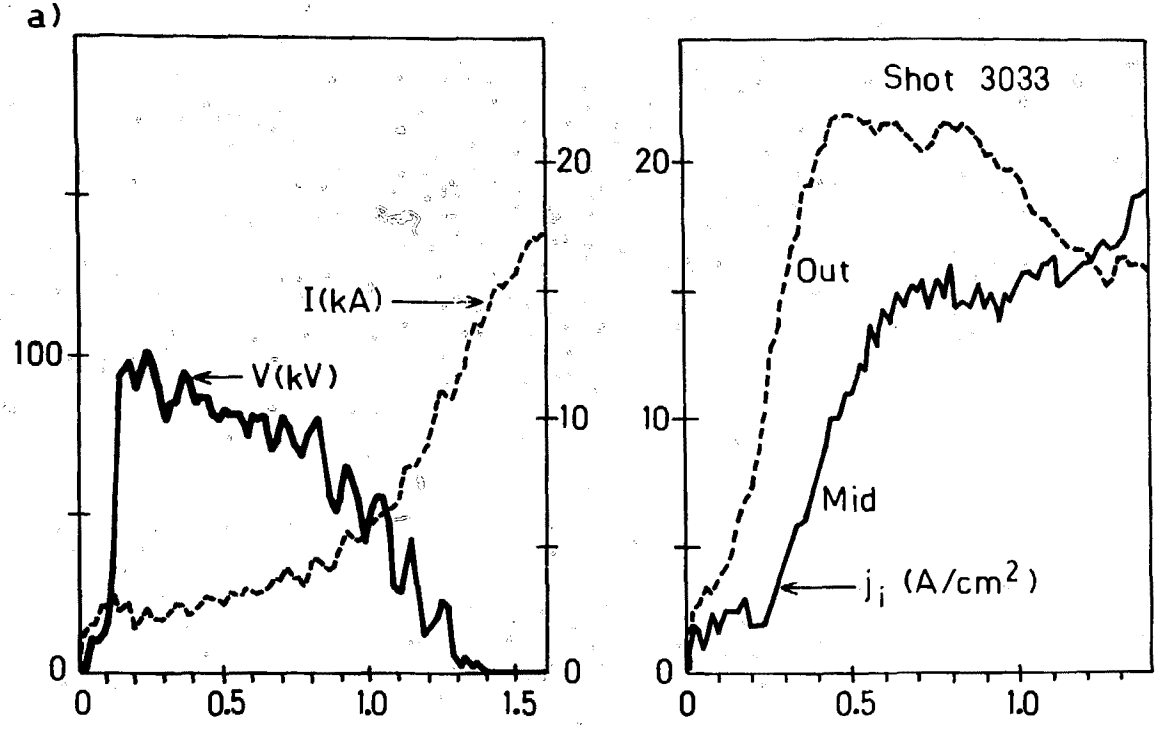
a)
I(kA)
V(kV)
100
0
20
10
0
0
0.5
1.0
1.5
Shot 3033
Out
Mid
j_i (A/cm^2)
20
10
0
0
0.5
1.0

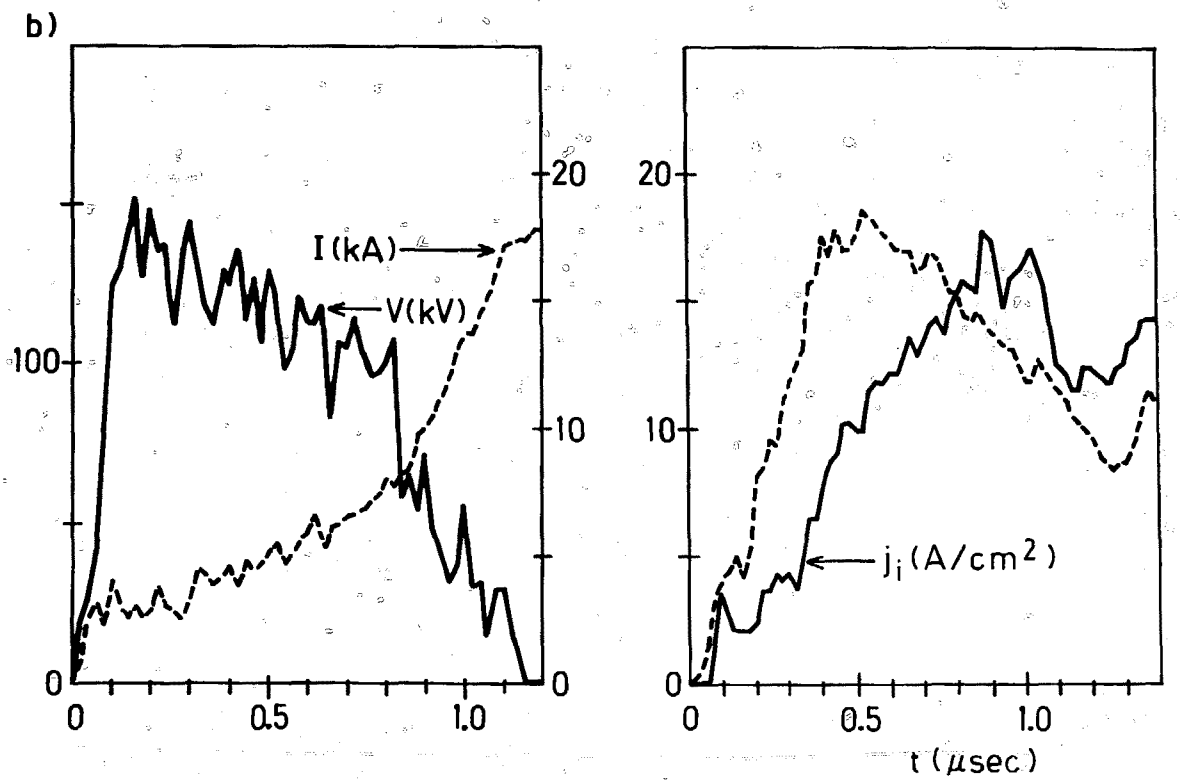
b)
I(kA)
V(kV)
100
0
20
10
0
0
0.5
1.0
20
10
0
j_i (A/cm^2)
0
0.5
1.0
t (μsec)

gap. Behavior of the gap under identical circumstances except with a 16 kV bank charge is shown in Figure 14(b). Reference to Figure 10 indicates that not only is the peak plasma flux reduced, but the arrival of the plasma is delayed 0.5 μsec compared to the 22 kV case. The results of this delay were evident in the experimental traces. At the beginning of the pulse, the voltage and current traces closely resembled magnetic insulation shots with no plasma injection (see Figure 11). Early in time, the ion current density probes showed no signal. At about 350 nsec the plasma apparently arrived, as indicated by a rapid change in the generator current and the appearance of ion signals in the probes. Following this, the current rose to the low equilibrium value typical of a 16 kV plasma bank charge. Another indication that the injector gap current was controlled by the injector plasma flow is shown in Figure 14(c). This case is the same as that of Figure 14(b) except the delay between firing the plasma gun and injector gap was increased from 2.9 to 3.4 μsec. The voltage, current and probe traces closely resemble those of Figure 10(b) except there is no initial zero current phase. The trace variations appear to be shifted forward 400 nsec to follow the incoming plasma flow.

Another scaling study was performed by maintaining the relative delay (3.6 μsec), the plasma bank charge (18 kV) and the Marx generator charge (40 kV) while varying the magnetic field strength in the gap. Probes were located 5 cm downstream viewing the middle gap. Results of these probe signals are shown in Figure 15. The magnetic field that penetrated the field excluder slots seemed to have a significant effect on plasma transport to the gap. This is indicated by the higher equilibrium current density levels at lower magnetic field. Also it should be noted that at the lower field values there were small signals in the downstream probes

FIGURE 14 Carbon ion injector shots, with plasma bank charge and timing varied. Plasma bank parameters: a) 22 kV, 2.9 μsec; b) 16 kV, 2.9 μsec; c) 16 kV, 3.4 μsec.

14 a)

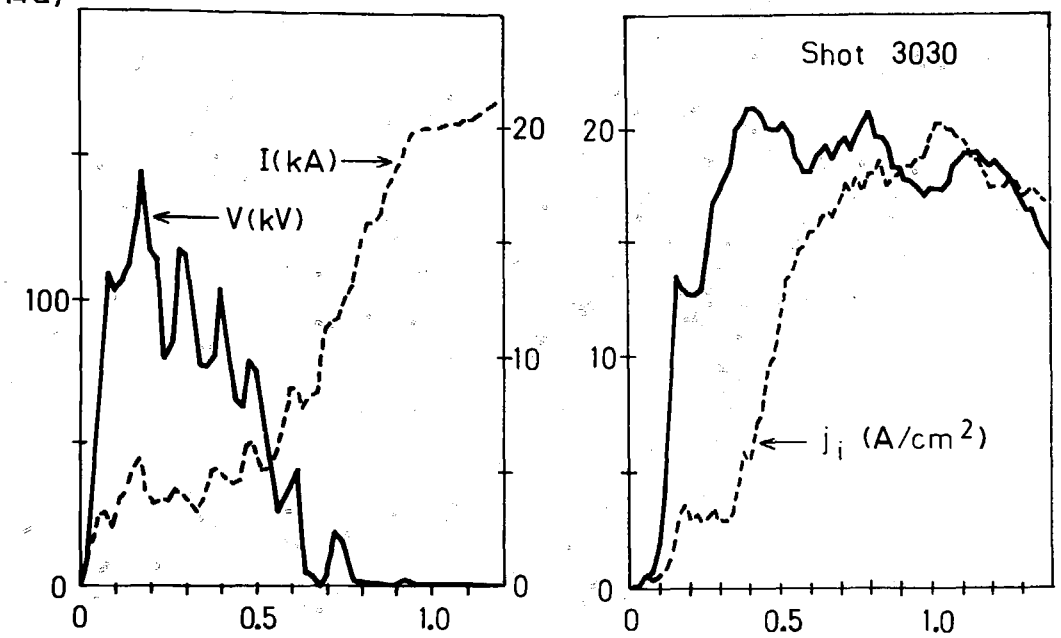

(4b)

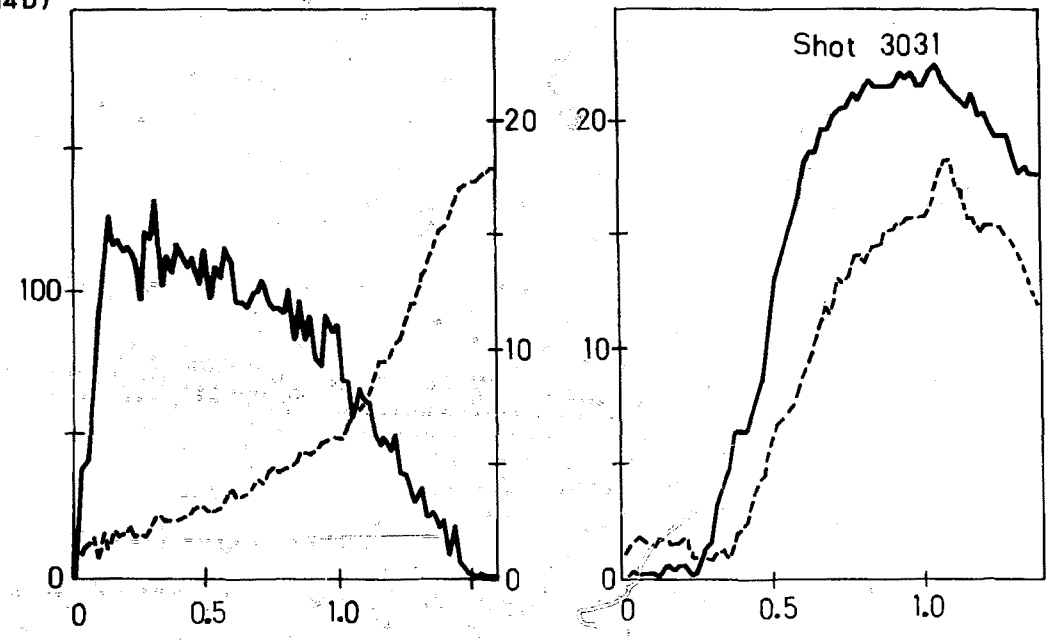

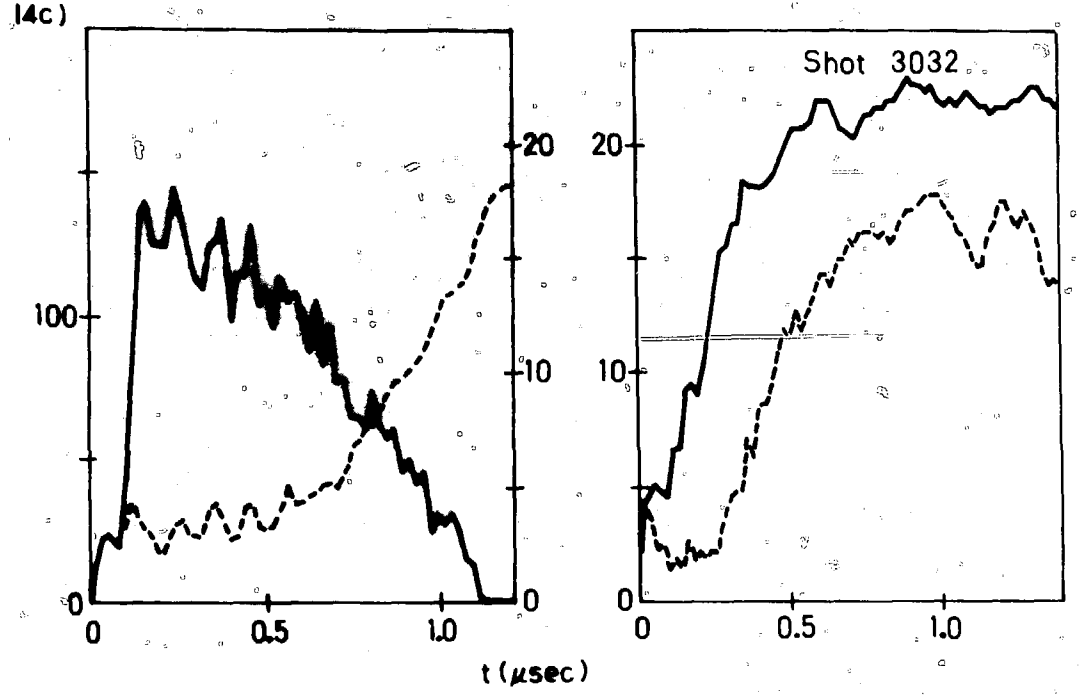
14c)
100
0
0
0.5
1.0
20
10
0
t (μsec)
Shot 3032
20
10
0
0
0.5
1.0

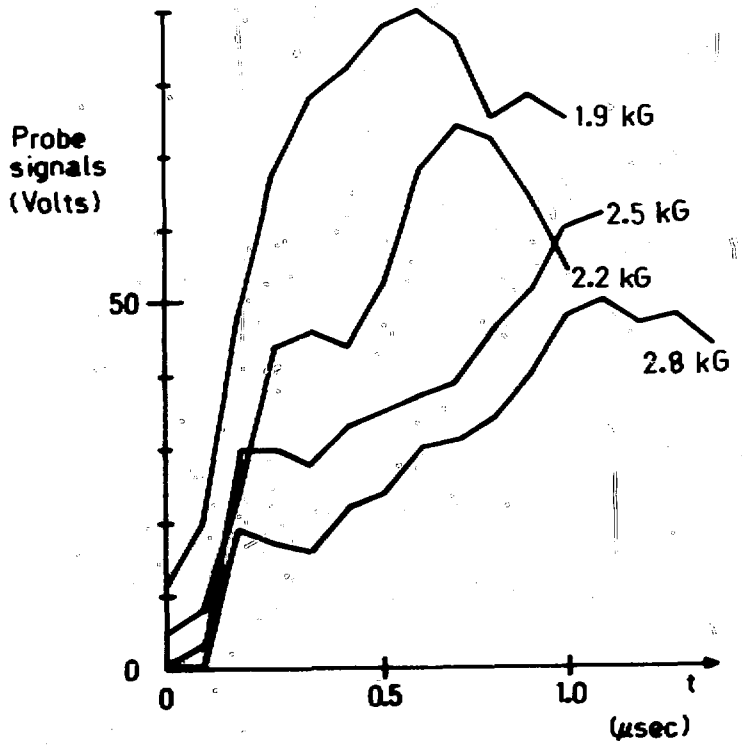

FIGURE 15 Carbon ion injector shots with magnetic field varied. Signals from probes located 5 cm downstream, viewing center slot. Marx generator charge: 40 kV, plasma bank charge: 18 kV, relative delay: 3.6 μsec. Ends of traces indicate times of gap shorting.

even before the appplication of the gap voltage at t = 0. These precursor signals were eliminated at the higher field values. Another interesting feature is that the rate at which the ion current density approached equilibrium was strongly affected by the magnetic field strength.

A final phenomenon of interest related to ion transport in the injector gap is the effect of plasma prefill. In the shot of Figure 12 the plasma gun-injector gap delay was adjusted so that the plasma arrived shortly before the gap was activated. There was thus a relatively small amount of plasma present in the gap. In contrast, for the shot of Figure 16 there was a longer delay (3.5 μsec) and a low gap magnetic field so that a plasma prefill could penetrate into the gap. The presence of a plasma was confirmed by probes 5 cm downstream which showed a small precursor signal. In this case, there was a longer initial low impedance phase with higher current since there was more plasma to be cleared. The most interesting feature is that the ion current density rose almost instantaneously to a high equilibrium level, in opposition to the case of low plasma prefill where it took a considerable time for the ion current density to reach saturation. The case of Figure 16 is similar to those in our initial report.[26] In these experiments, an undamped Marx generator was used and there was a considerable current during the low impedance phase. During the impedance transition, there was a large voltage overshoot driven by the generator inductance, often exceeding 300 kV. A number of tests were performed to determine the composition of the emerging beam with regard to ion species. Time-of-flight studies similar to those of Figure 9(b) were carried out and reported in a previous reference.[26] Downstream probe signals showed a very small proton precursor and sharp lines indicating bunched C^{+} and C^{++} packets form the rising gap voltage. The data were consistent with about equal current fluxes

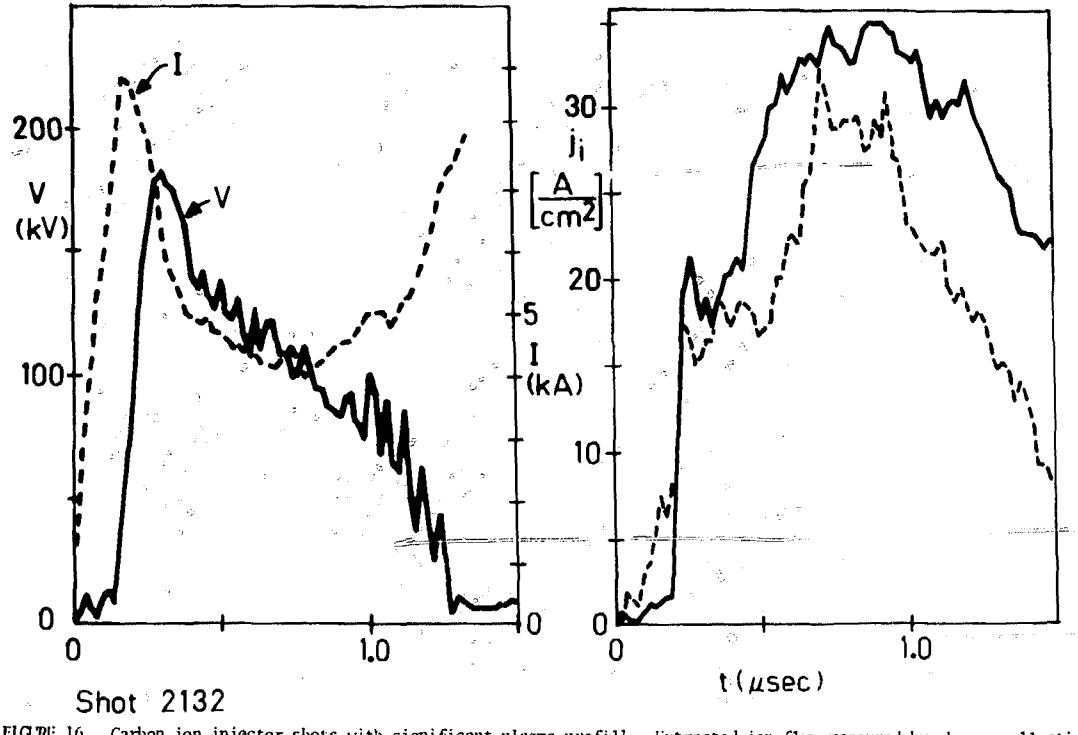

FIGURE 16 Carbon ion injector shots with significant plasma prefill. Extracted ion flux measured by charge collecting probes, 5 cm downstream.

of the two carbon ions. Measurements were taken with a Thompson parabola mass spectrometer which were generally in agreement with these findings. The mass spectrometer results will be discussed in detail in Section V. Measurements made with the magnetic spectrometer are shown in Figure 8(b). Ions were detected only in the undeflected channel, indicating an absence of protons.

A final quantity of interest was the quality of the beams extracted from the carbon injector. This was of particular concern since in early tests the beam was brought to an annular line focus only 5 cm from the virtual cathode and thus was not useful for linear accelerator injection. In these experiments, a single slot of width 2.5 cm centered on the average annular radius was used. The line focus was clearly indicated by witness plates placed at varying distances downstream. Current densities measured at downstream locations were consistent with ions diverging from the focal point. At the initial location of the post-acceleration gap (60 cm from the injector) the current density was only about 10 percent of its injected initial value. The strong focusing was attributed to the electrostatic optical effects of curved virtual electrodes which resulted from the bulging of magnetic field lines into the large extraction slot. To correct this, a field excluder with three smaller slots (0.9 cm width) was constructed, as shown in Figure 3. This reduced the distortion of magnetic field lines considerably.

Initial measurements were performed using polished lucite witness plates 12.7 cm downstream from an aperture array. Ordinary witness plate materials and calorimetry were not very useful for the low energy carbon beams. Because of the extremely short ion ranges, a microscopic layer was blown off, coupling little energy to the target. On the polished lucite

plates, areas of ion bombardment appeared as cloudy patches when properly illuminated. The aperture plate was located 2.5 cm downstream from the virtual cathode plane. Some null tests were performed, and it was confirmed that there was no damage unless the entire system was fired (plasma guns, insulating field, and injector voltage). Also, no damage appeared behind apertures facing the field excluder structure rather than the extraction slots. In the series of shots taken, the injector Marx generator charge was 40 kV, the applied field was 2.5 kG, the plasma gun bank charge was 18 kV, and the delay to injector gap initiation was 3.2 μsec. This was a relatively short delay time, so there was little plasma prefill. In this case, we expected more energy extraction from the outer slot since it reached current saturation before the other slots. This was confirmed by observations of enhanced damage on the aperture plate front face at the outer radius. It was possible to measure boundary divergence angles by comparing the size of the damage spots on the downstream plate to the size of the apertures. The results when averaged over sixteen apertures are boundary half angles of $1.3 \pm 0.6°$ in the azimuthal direction and $3.4 \pm 1.3°$ in the radial direction. These are upper limits since it is uncertain what fraction of the beam spreading is attributable to inherent divergence and what fraction to residual space charge effects. The larger spreading in the radial direction was probably due to bulging of the field lines into the gaps. In a new system under construction, the magnetic field will have a faster risetime which will allow finer slot structures to be used. In any case, the radial defocusing effects were considerably reduced from the 14° spread characteristic of the single slot design.

It was also possible to estimate the beam divergence from downstream current density measurements. This gave an upper limit, since there were a

number of possible factors affecting beam propagation, such as longitudinal spreading from a velocity spread, beam losses to produce neutralizing electrons (see Section IV), and possible residual space charge effects. The predicted downstream current density from the three slot injector is shown in Figure 17 for various values of $z\Delta\theta_b/w$, where z is the distance from the injector, $\Delta\theta_b$ is the boundary half angle of divergence, and w is the width of the extraction slot. To simplify this calculation, a one-dimensional approximation was used with slots of infinite extent in the direction perpendicular to r and z. This is a good approximation when $z\Delta\theta_b \ll R_d$, the average gap radius. Measurements were taken using an array of 3 probes distributed radially at a point 3 cm downstream from the location of the post-acceleration gap, a total of 32 cm from the injector. A radial average of the ion current density was calculated at a time corresponding to the arrival of ions from the saturation phase of the injector. There was no applied voltage or magnetic field in the post-acceleration gap (see Section IV for effects of applied magnetic fields). The average ion current density multiplied by the 300 cm^2 area of the dirft annulus gave a total current about 70 percent of the injected ion current. Referring to Figure 17, this corresponded to a radial $\Delta\theta_b$ of about 4.5°, consistent with the witness plate results considering the limited accuracy of the measurement. In this case, $z\Delta\theta_b$ was 2.5 cm compared to the injector radius of 10 cm, so the assumption underlying Figure 17 should hold.

The greatly improved divergence and parallelism of the beam from the carbon injector strongly indicated the presence of virtual cathode effects. In the absence of an electron cloud, the ions would diverge toward the real electrodes at the radial peripheries. The quality of the beam also indicated that there was an electron distribution in the acceleration gap that had a

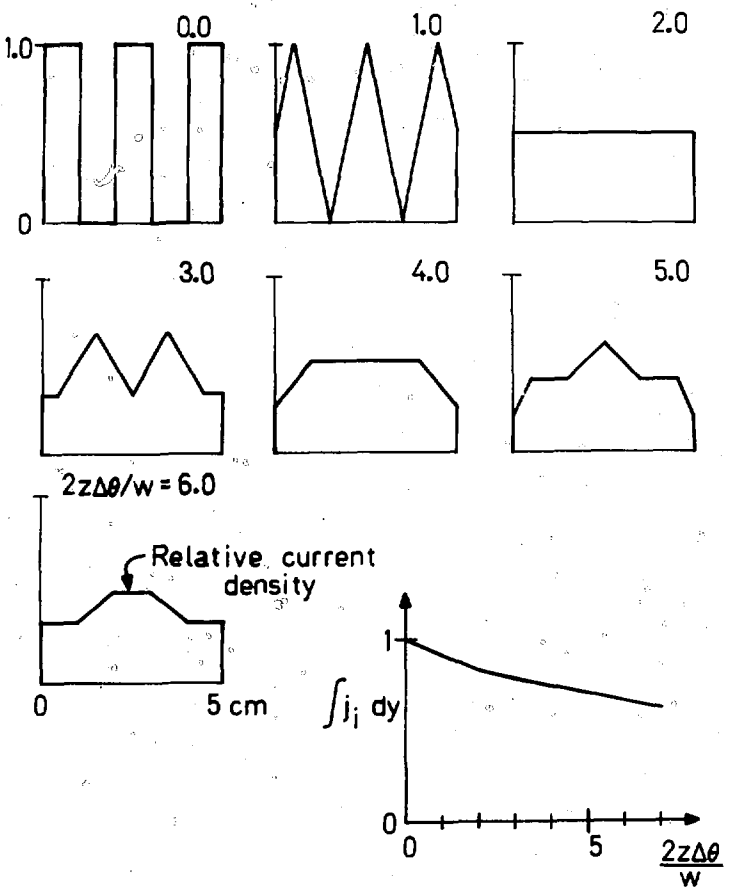

FIGURE 17 Predicted relative downstream current density for three slot carbon injector. The transverse velocity distribution is that described in footnote 35; $\Delta\theta$ is the boundary half angle of divergence. The annular injector has been approximated as an infinitely long slit. Longitudinal distances are given in terms of the dimensionless quantity $2z\Delta\theta/w$, where z is the distance downstream and w is the width of one of the three slots.

strong influence on transverse space charge effects. For comparison, we can calculate the radial divergence of one of the three extraction slot beams assuming the beam has no electron neutralization while crossing the gap. This would be the case if the magnetic gap were ideal, having the electron cloud closely confined to the cathode region. Included in the calculation is the presence of image charges in the virtual electrodes, which cancel a good fraction of the average radial fields. Assuming a 0.7 cm physical gap and a C^+ beam of width 0.95 cm at 20 A/cm^2 and 100 keV, the radial divergence is predicted to be 30°, ten times higher than that observed.

D. Model of Injector Behavior

At this point, we will consider whether a consistent explanation can be advanced to account for the factors affecting ion flow in both the proton and carbon injectors. We will first consider a possible explanation, and then discuss how this model can account for the unusual features of the two injectors. The concept of ion current density enhancement generally refers to methods of obtaining controlled ion flows in a vacuum gap greater than the predicted by the Child-Langmuir law. The simplest example of an enhancement over single species ion flow is Child-Langmuir bipolar flow, where there is a counterflow of ions and electrons in a one-dimensional gap. If the particles start from rest, the cathode is at zero potential, and the anode is at some V_o, the particle densities vary as $n_e \sim \phi^{-1/2}$ and $n_i \sim (V_o - \phi)^{-1/2}$. In this case, the total number of electrons and ions in the gap must be equal, since the electric fields are zero at both electrodes. For the non-relativistic case, the current densities are in the ratio $j_i/j_e \sim (m_e/m_i)^{1/2}$ since the electrons move faster. The ion current density is increased a factor of 1.86 from the single species value.

A simple gap like this has little improvement in current density and a very low efficiency for ion acceleration. Since the ions travel in a relatively straight line and exit the gap in one pass, there is little that can be modified in their behavior to improve the situation. The key to improvement is in the control of electron flow. By increasing the residence time of electrons in the gap, the efficiency can be increased. The ion current density is increased by allowing the electron distribution to relax from the $\phi^{-1/2}$ case. When this happens, there is more negative space charge near the anode where the ion current density peaks, thus reducing some of the space charge constriction.

The most familar example of ion current density enhancement is the reflex triode.[39,40,41] Good efficiency results from the fact that, if the anode has transparency T, the electron must travel a distance $(1 - T)^{-1}$ times the gap spacing to reach the anode. If stochastic processes are allowed (such as scattering from an anode foil) the electron distribution relaxes from the monoenergetic case, allowing the extraction of almost unlimited ion current density. Enhancement mechanisms in magnetically insulted diodes have not been treated as extensively as those in the reflex triode. Theoretical treatments have certered on cathode produced electron distributions which are delta functions in canonical momentum perpendicular to $\vec{E}$ and $\vec{B}$ and/or delta functions in energy.[33,34] These models show that at practical magnetic fields relative to the critical insulating field, $(B/B^* > 1.5)$ ion flow is very close to the Child-Langmuir limit. The ideal one-dimensional magnetically insulated gap has space charge limited ion flow and 100 percent efficiency because of the infinite electron residence time. Such behavior has been observed in highly symmetric gaps pulsed for short times,[8,24] but a number of experiments violate the conditions of

these models and have shown enhancements over an order of magnitude. These experiments typically have perturbed electron flow because of converging electron orbits,[11,29] perturbed magnetic field drifts due to the gap current feeds[12,32] and geometrical variations and discontinuities in the electron drift direction.[29] The general effect of these asymmetries is to push electrons off the cathode towards the anode.

In the present experiment, the electron cloud is quite stable, a consequence of good symmetry along the electron drift direction. A measure of the success of the magnetic insulation is the fact that the electron leakage current is less than a few hundred amperes compared to predicted currents on the order of 50 kA for uninhibited flow. Nonetheless, even with good stability, there are two possible mechanisms that could cause the electron distribution in the experiments reported to differ from that of the ideal magnetically insulated diode. The first is the use of a plasma prefill. When the gap voltage appears, the plasma ions flow out, but many of the plasma electrons could be trapped by the magnetic field. In this case, the gap is supplied with an initial source of electrons distributed in position, rather than from the cathode only. The second possible factor is the presence of weak stochastic processes which cause a diffusion of the electron distribution toward the anode. This diffusion could result from RF oscillations or from small azimuthal asymmetries which break the conservation of canonical momentum. The observed leakage current reductions imply that electrons are confined for more than 300 orbit times, so diffusional effects might be expected to appear over time scales long compared to 30 nsec. Relaxation of the electron distribution from one peaked near the cathode would allow more electrons to enter the gap, increasing the ion flow which, in turn, allows the electron distribtuon to grow. This process would bootstrap unless some limit were reached.

We can now consider how this model can explain a number of features of ion flow in both the proton and carbon injector configurations.

1) At early times, both the proton injector and the carbon injector with no plasma prefill exhibited low current densities characteristic of space charge limited flow. The ion current density was sensitive to the physical gap spacing and followed variations in the voltage. This behavior was typical of the ideal magnetically insulated diode. This was expected since the source plasma was localized at the anode, the only possible source of electrons was the cathode, and the applied magnetic field was well above B*. This mode of operation persisted for time scales on the order of 0.1 μsec.

2) In the proton injector, the azimuthal uniformity of ion emission was observed to improve considerably at latter times. This supports the idea that the electron distribution is the chief controlling factor in ion current flow. The electrons were the only agents in the gap that communicated azimuthally and, in order to be in equilibrium, the electron flow would seek to maintain uniformity along the drift direction.

3) From past experience with flashboards, the anode plasma in the proton injector was very dense and capable of supplying a practically unlimited ion current density. The consequence of this was evident in measurements of long time scale shots. The current and ion current density climbed slowly and steadily, with no apparent limit, even though the voltage was constant or slowly decreasing. Late-time local current density enhancement over 100 times the Child-Lagnmuir limit were measured.

4) Although the main component of the electron drift velocity was in the azimuthal direction, they were also free to move parallel to the radial field lines under the action of various forces. Early in time the electron

cloud near the cathode would tend to be spread uniformly in radius because of space charge repulsion. Indeed, the ion emission in the space charge limited phase was observed to have good radial uniformly. Later in time, though, when the transverse space charge forces in the proton injection gap were reduced by relaxation of the electron distribution, it might be expected that the magnetic fields would have a larger effect on the radial orbits. Inspection of Figure 1 shows that the curvature of the gap magnetic field lines forms a radial mirror that would tend to center electrons on the average annular radius. In general, the flashboard can supply plasma at any point, so the bootstrapping process would tend to grow most rapidly at the electron equilibrium radius. Perturbing this general trend was the fact that the flashboards could develop hot spots that ignited earlier or more intensely. The growth of particle flow could develop most quickly at these spots, neutralizing space charge effects and producing competing forces with the magnetic mirroring. Electron orbits would then consist of an azimuthal drift centered mainly at the point of maximum field concavity with radial excursions induced space charge forces to emphasize the points of maximum ion flow. This may explain the unusual behavior of the radial variations of ion emission in the proton injector. The presence of anode hot spots caused by particularly sharp pins, protrusions, etc. may account for the reproducibility from shot to shot.

5) The diffusion of electrons across a magnetic field is strongly affected by the magnitude of the field. The electron diffusion rate should in turn determine the growth of ion current density. This effect is certainly in evidence in the data of Figure 6, Figure 8, and Figure 15. This behavior was also shown on a local basis in the carbon injector

since the outer slot (where $\int B_r dz$ was a minimum) showed the fastest ion current density risetimes. In this configuration, because the extraction slots were separated by substantial regions inaccessible to ions, it would be expected that there would be three separate diffused electron clouds.

6) In the carbon injector, the maximum flux of ions was determined by the plasma guns. In the case where there was no plasma prefill, (see, for instance, Figure 14(b)) the ion current density rose over about the same time scales as the proton injector, but then clamped at an equilibrium level close to the measured plasma flux. Apparently, the same process of electron diffusion took place until the gap could pass all entering ions. This process took place fastest in the outer slot where the magnetic field was lowest. Ion source limitation of the gap current density also explains why there was radial uniformity of ion extraction at saturation between the three slots, as opposed to the proton case where the current density was strongly peaked.

7) With a significant initial plasma prefill, the carbon injector appeared to immediately enter the saturation mode after the initial low impedance phase. This probably resulted from the presence of the precursor electron distribution.

The only possible competing explanation for the ion enhancement we observed is plasma gap closure. This effect is often observed in relativistic electron beam diodes. Plasmas produced on the electrodes expand, thus reducing the width of the vacuum gap. There are a number of reasons why this process probably is not important in the present experiment. First, considering the proton injector, plasma closure would worsen, rather than improve, azimuthal uniformity late in time. Also, we would expect to see

the maximum late time current density at the outside annular radius rather than the average radius, since the magnetic field is weakest at this point and plasma should be initiated there preferentially because of the sharp anode edge. Neither of these effects agrees with observation. Also, it is unlikely that the smooth, steady variations of perveance are accountable by an actual change in the physical gap spacing. At later times, the gap would not even be magnetically insulated if this were the case. Arguments about gap closure in relation to the proton injector are given in detail in reference 30. Tests with the carbon injector provided a fairly definitive demonstration that gap closure effects were negligible. Referring to Figure 3, the physical cathode in this case consisted of 0.3 mm hoops at the inner and outer radii. It is unlikely that cathode plasma expansion from these edges could have much effect, particularly on the center slot. There were apparently no anode plasmas at all. This was attested to by the fact that ion current was detected only at the slot locations, the ion current clamped at the value determined by the remote plasma guns, and downstream diagnostics showed fairly pure carbon ion beams.

The implications of the electron diffusion model for the operation of practical, high current magnetically insulated gaps are far reaching. The plasma fill experiments demonstrated that symmetric gaps could be preconditioned with an initial electron fill to pass very high ion fluxes. Most important, these fluxes were obtained without sacrificing the efficiency of the gap. If the average diffusional velocity of the electrons is low, the injector can have a relatively high density of neutralizing electrons with small leakage current. The operation of these injectors in a source limited mode was a unique case because the gap ran in an enhanced mode with controllable impedance. By eliminating the dependence of current on gap voltage,

such injectors could be matched to pulse-forming-networks with very high efficiency.

IV. NEUTRALIZED PROPAGATION OF ION BEAMS

The theory of automatic ion beam neutralization by low energy electrons emitted from surrounding conducting boundaries has been mentioned briefly in Section I. In this section, we will discuss the theory in more detail and review the measurements we have been able to make on this phenomenon. Considering the theory, two special cases have been treated: neutralization in the presence of transverse magnetic fields which prevent longitudinal motion of the electrons,[21] and one-dimensional neutralization in free space.[22] In the first case, peripheral electrons must be supplied on all the field lines which the ion beam crosses. These electrons are pulled into the beam volume along the field lines by the ion space charge fields. This process has been studied by a computer simulation of electron beam dynamics in the geometry shown in Figure 18. It was found that during the rise of the ion beam density, free electrons were pulled into the beam with a flow determined by vacuum space charge considerations. Because of the light electron mass this flow could be rapid, providing neutralization on nanosecond times scales. An essential part of effective neutralization was the introduction of asymmetries into the ideal one-dimensional model. These asymmetries, which were typical of real systems, brought about randomization of electron orbits which caused them to be trapped in the ion beam volume. During the rise of the ion beam density, a residual positive potential was needed to attract electrons to balance the change in the number of ions in a cross sectional element. Physical arguments in agreement with the computer calculations[21] gave the potential at the center of the drift space of Figure 18 as

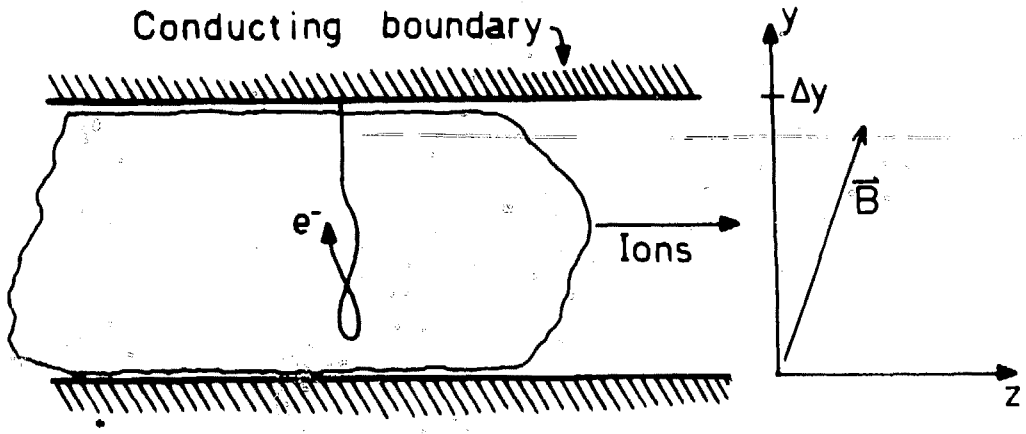

FIG. 19 Geometry pertaining to the autogytic neutralization of high intensity ion beams propagating in regions of transverse magnetic fields.

$$\phi_r(0) \simeq [(9\pi/4)(n_{io}/\Delta t_r)e\Delta y^3 / \sqrt{2e/m_e}]^{2/3} \qquad (1)$$

where n_{io} is that final density of the uniform beam reached after a linear rise over time t_r. The transverse dimension of the drift space, y, is defined in Figure 18. After the rise in n_i terminated, the residual potential dropped to zero within a few electron transit times, which were typically subnanosecond. A total balance of electron and ion density was thus achieved automatically.

In the second case,[22] longitudinal neutralization in regions with no applied fields was treated. In the model, an ion beam of infinite transverse extent passed through a conducting foil or mesh which supplied low energy electrons. It was shown that a self-consistent sheath solution existed such that electrons were accelerated to move forward with the beam providing neutralization of both the space charge fields and the beam current. The longitudinal potential rise across the sheath was of the order of $4(m_e/m_i)E_B$, where E_B was the ion energy. The actual situation in the experiments in question was probably a mixture of the two special cases. In regions near the acceleration gaps where there were transverse magnetic fields, the first model was directly applicable. In other regions, electrons could move longitudinally, although they were pulled in transversely from surrounding boundaries since there were no physical grids in the experiments. The potentials necessary to attract electrons from the boundaries were generally higher than those necessary to give the electrons a longitudinal velocity equal to that of the ions (5-20 V), so the residual potentials, even in the case of no transverse field, were probably of the order of those given by Eq. 1.

Typical space charge potentials can be estimated for the experiments by substituting characteristic values in Eq. 1. For instance, considering 120 keV C^+ with a maximum current density of 20 A/cm^2, the maximum density, n_{io}, is about 10^{12} cm^{-3}. With risetime of 0.2 μsec and a transverse dimension of 1.5 cm, the residual potential during the beam risetime is found to be 4 kV. For these same parameters, the central potential for an unneutralized beam would theoretically be 2 MV. Thus, an unneutralized beam would have such large space charge fields that it could not propagate at all. The ions would be turned by longitudinal fields less than 2 mm from the cathode. From these arguments, if automatic neutralization proceeded according to theory, the fractional imbalance of space charge in the beam should be less than 0.2 percent.

The subject of the origin of boundary electrons has not yet been addressed. We have the capability of providing electrons from large area, pulsed sources.[28] We have not yet been able to demonstrate the effect of these sources because electrons sufficient for propagation appeared to be produced automatically. The most probable source of free electrons was secondary emission resulting from collisions of ions with the surrounding boundaries. This could have occurred because of inherent beam divergence or blowup of the unneutralized head of the beam. Calculations on this effect are presented in Appendix II. The result of these calculations is that secondary emission processes can provide a sufficient source of electrons for propagation. Sufficient in this case means that the loss of ions necessary to produce the electrons should be undetectable for the propagation distances and pulselengths in question.

To the present, we have been able to make only passive observations of downstream current density to compare with theoretical predictions. This

was due in part to the difficulty of performing diagnostics at the elevated potentials of the dirft tubes and to the lack of control over electron production because of ubiquitous secondary emission processes. A further limitation was that it was not possible to measure residual potentials directly. This came about because of theoretical limitations; the probe itself would emit electrons that would perturb the potential.[29] Nonetheless, current density measurements are useful since the ions orbits are very sensitive to an imbalance of space charge and allow an estimate of the upper limit of non-neutralization.

As mentioned in Section III, with a three slot carbon injector and with the beam confined in an annular region of radius 10 cm and width 4.8 cm, about 70 percent of the beam arrived at a location 32 cm downstream. It is evident that a strong neutralizing process took place, since propagation of the bare beam would be limited to a distance of 0.2 cm. We can arrive at a more quantitative picture by considering a beam of uniform density C^+ ions at 120 keV of width 4.8 cm. If the beam is approximated as of infinite extent in the direction perpendicular to r and z, it is a simple matter to calculate laminar particle orbits to determined how the space charge must be modified to account for the observed downstream current density. With an average initial current density of 10 A/cm^2, the charge density would have to be reduced by a factor of 500 from the bare beam case to account for the small losses. Beam divergence effects have been neglected, so this is an upper limit on the charge imbalance. Note that the space charge effects are less than or equal to the upper theoretical limit. Similar considerations apply to the witness plate tests described in Section III. The width of the beam signature 13 cm downstream was increased in the azimuthal direction by only 0.3 cm with an average current density at the

aperture of 20 A/cm^2. The radial and azimuthal aperture dimensions were 0.95 cm and 1.2 cm respectively. These figures again combine to give an upper limit on charge imbalance of 0.2 percent.

A certain degree of control could be exerted over the propagation of the beam by the application of the magnetic field in the post-acceleration gap. This was done with no applied electrical field. This could have two effects on beam neutralization. First, the presence of transverse field lines meant that electrons had to be supplied locally in the region of the post-acceleration gap. According to Appendix II, this should have had a small effect on beam propagation. Of greater importance was the fact that the second gap was magnetically insulated. In this narrow region, electrons could not be supplied directly along field lines. The beam current density in the gap was about 6 A/cm^2 when using the three slot carbon injector with 30 cm intergap spacing, implying that $n_i \sim 3 \times 10^{11}$ cm $^{-3}$. The gap width was 1 cm, so the maximum potential at the gap center was about 70 kV in the absence of electrons. The beam could thus cross the gap, but there would be strong transverse space charge forces resulting in angular deflection on the order of 30°.

The effect of the post-acceleration gap magnetic field on the measured current density downstream from the gap was measured in a variety of circumstances. Typical data taken with a charge collector 3 cm from the gap are shown in Figure 19. Two cases are shown, with and without a 2.5 kG field taken on successive shots with injector parameters maintained constant. Note that in the case with applied field, the rise in current density exhibits a delay on the order of 200 nsec. Although the final current density attained in the applied field case is somewhat lower than the field free situation, it is considerably in excess of that expected if there were

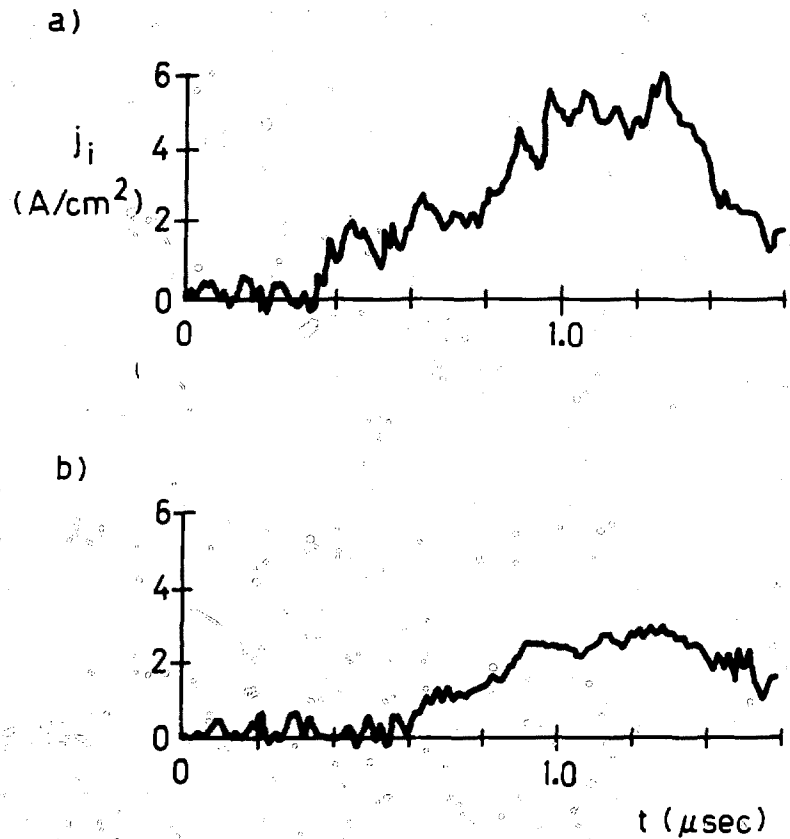

FIGURE 19 Charge collector data showing effect of post-acceleration gap magnetic field on ion beam propagation. Carbon injector; 30 cm intergap spacing; probes 3 cm downstream from second gap. a) No applied magnetic field in second gap. b) Second gap magnetic field equal to 2.5 kG.

a complete absence of electrons in the post-acceleration gap. The probable cause of this behavior is that negative space charge collected in the second gap in a manner analogous to the injector. The unneutralized electrical field stress of 140 kV/cm was comparable to that applied to the injector, resulting in a similar process of electron diffusion into the gap. Since there was no applied electric field, these electrons could be trapped easily. The delay in the rise of the downstream current density could be representative of the relaxation time of the electron distribution.

V. POST-ACCELERATION OF HIGH INTENSITY ION BEAMS

In this section, we will discuss the use of a second magnetically insulated gap to increment the energy of multi-kiloampere ion beams. The major concern will be the change in longitudinal velocity; transverse deflections and focusing effects in the gap will be treated in Section VI. A number of system and diagnostic configurations were used over the course of the experiments. The Pulselac A system as originally conceived was a five stage accelerator with resonant electrostatic drive. The gaps were to be powered by synchronized floating Blumlein lines that applied relative voltages between drift tube sections. The drift tubes were designed to be fairly long (60 cm) to relieve requirements on pulselength and synchronization. After gaining experience with the properties of the injectors and an additional gap, it became evident that it would be impossible to contain a significant fraction of the beam in the low velocity accelerator with large gap spacing. For this reason, a new five stage system (Pulselac B) is presently under construction. This accelerator should be capable of accelerating beams to 1 MeV with only 7.6 cm between gaps. The low divergence beam emerging should then be suitable for transport in a long gap system.

In regard to the present experiments, tests were performed with only one post-acceleration gap. Initial tests were done using the original 60 cm intergap spacing. Both the proton and carbon injectors were used in these tests. Because of the large currents available from the proton injector towards the end of the pulse, over 2 kA of ion current was measured at the second gap despite the long narrow drift region.

The single slot carbon injector was used in initial experiments. The sharp focus near the cathode produced a diverging beam. In this case, the second gap ion current was limited to a few hundred amperes. The bulk of the data from the Thompson parabola mass spectrometer was taken in this configuration. Experiments were performed with the post-acceleration gap voltage applied by both floating Blumlein lines and direct connection to the second Marx generator. In a second series of experiments, the system was modified in order to post-accelerate a significant current of carbon ions. The injector was changed to three slot configuration and the second gap assembly was reversed so that the intergap spacing was 30 cm. In these tests, over 2 kA of carbon ions crossed the gap with an applied voltage of about 200 kV.

The Thompson parabola mass spectrometer[42] measured the distribution of ion species and the energy spectrum of the extracted beams. This device consisted of a series of apertures to collimate the beam, a region of transverse electric and magnetic fields parallel to each other, a drift region, and a 7.6 cm Channel Electron Multiplier Array to act as an ion image detector. Secondary electrons produced at the entrance to the CEMA were multiplied in the channels and then accelerated to a phosphor, which was directly coupled to photographic film through a fibreoptics window. The magnetic and electrical deflections were at right angles to each other and were given by

$$x(\text{electrical}) = (3.6 \times 10^2) Z V_p / E_B \quad , \qquad (2)$$

$$y(\text{magnetic}) = ((3.7 \times 10^6) Z^2 / A E_B)^{1/2} \quad .$$

The deflections are given in cm, Z is the ion charge state, A its mass number, and E_B its energy in eV. The quantity V_p is the voltage applied to the deflection plates.

In practice, it was necessary to maintain the spectrometer at ground potential since it required its own vacuum pumping station. This caused some complication since the beam was extracted at a high negative potential. In order to solve the problem, we took advantage of the sensitivity of the spectrometer and separated it from the high voltage terminal of the experiment by a long, insulating tube. A glass pipe 30 cm in diameter and 152 cm long was used. The length was sufficient so that the applied voltage pulses were shorter than the ion transit time. Even though the ions were produced and measured at ground potential, they gained an energy determined by the sum of the electrostatic voltages on the gaps. In this sense, the system could be considered as an actual multistage accelerator. In practice, the injector was fired and the activation of the second gap was delayed to allow the propagating current to rise and to compensate for the ion propagation time between gaps. This propagation time was typically 140 nsec for p^+ and 500 nsec for C^+. External breakdown phenomena typically shorted the injector voltage within 0.1 to 0.2 μsec of the activation of the post-acceleration gap. The maximum pulselength of the second gap was about 0.2 μsec. The transit time of the beam from the second gap to the grounded end of the glass pipe was 0.22 μsec for p^+ and 0.76 μsec for C^+ at the maximum energy of 300 keV. Thus there was a good chance that both gaps were shorted at the arrival time of the proton beam at the spectrometer; this was almost a certainty for carbon.

Data taken with the Thompson parabola mass spectrometer are shown in Figure 20 along with voltage waveforms from the first and second gaps. Because of the difficulty in reproducing the photographic output, the images have been traced in ink. Also shown are predictions of the positions of various ion species using Eq.'s 3. An example of the original data is included in Figure 20(e). The data of Figure 20(a) corresponds to a shot with the carbon ion injector and no applied voltage on the post-accelertion gap. There were no damping circuit elements in the injector Marx generator, so that the rapid rise of impedance following the gap clearing phase caused an inductively driven voltage overshoot up to about 225 kV. Subsequently, the voltage returned to the 80-100 kV range. The origin of the x-y plane in Figure 20(a) was clearly marked by the signature of high energy neutral atoms produced by charge exchange processes during transit. There was a well defined C^{+} line and a fairly weak indication of C^{++}. In addition, there was a line corresponding to copper ions, probably produced by erosion of the plasma gun electrodes. The relative brightness of the lines is not a reliable indication of the flux of different species. Effects such as the variation of the secondary emission coefficient at the multichannel plate enetrance, non-linearity of the recording film, and saturation of the multichannel plate and phosphor could all enter.

In the lines of the three species present, there were visible regions corresponding to the energy of direct electrostatic acceleration. However, on the C^{+} and Cu^{+} lines, there were indications of particles at double the injector voltage drop. In the case of copper, there was even a bright region corresponding to particles with triple the energy. This phenomenon was due to charge exchange with the background gas in the 3 meter distance from injector to detector. The equilibrium fractions of carbon ions passing

FIGURE 20 Thompson parabola mass spectrometer results. Shown are reproductions of photographic output, with plots of first and second gap voltage waveforms. Lines are predictions (with no free parameters) of various ion species lines. a) Carbon ion injector, no post-acceleration. Inductively driven voltage overshoot. b) Carbon ion injector with capacitive damping. No post-acceleration. c) Damped carbon ion injector with post-acceleration. d) Proton flashboard injector with post-acceleration. e) Original photographic data of case (d).

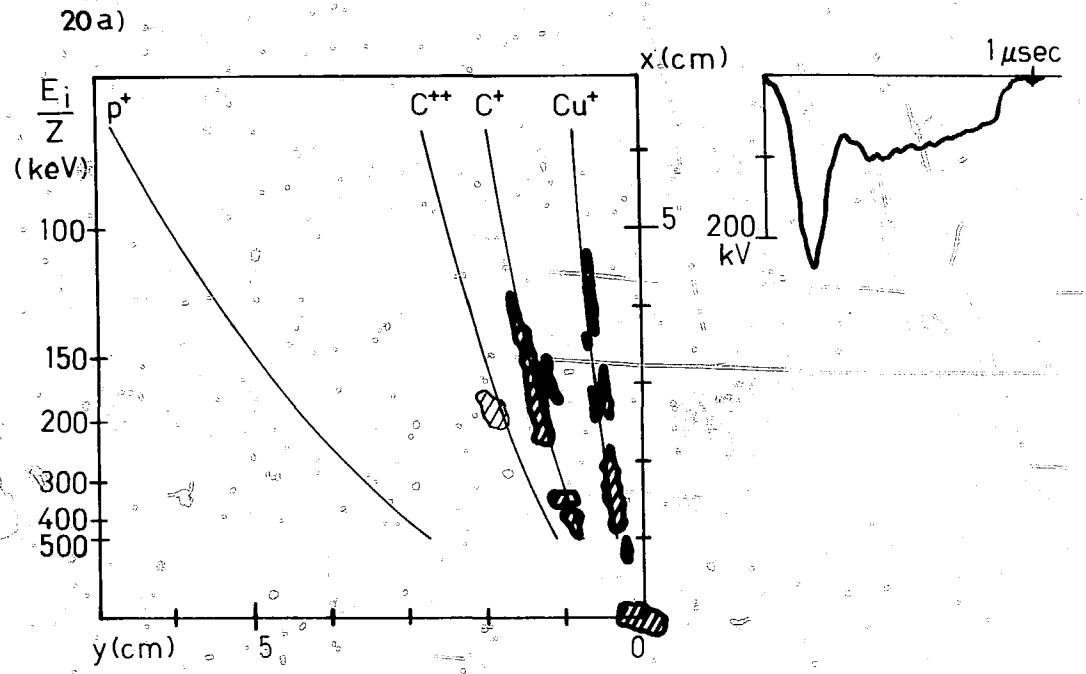
20 a)
$\frac{E_i}{Z}$
(keV)
100
150
200
300
400
500
p+
C++
C+
Cu+
x(cm)
5
0
y(cm)
5
0
1 μsec
200
kV

20b)

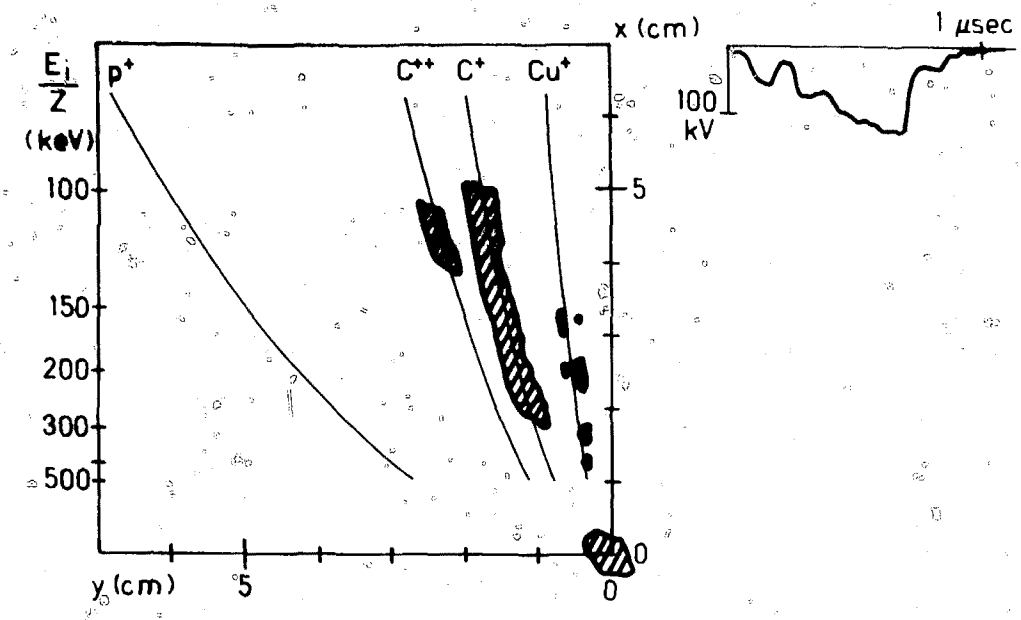
x (cm)
1 μsec
100 kV
$\frac{E_i}{Z}$ (keV)
p+
C++
C+
Cu+
100
150
200
300
500
5
0
y (cm)
5
0

20c)

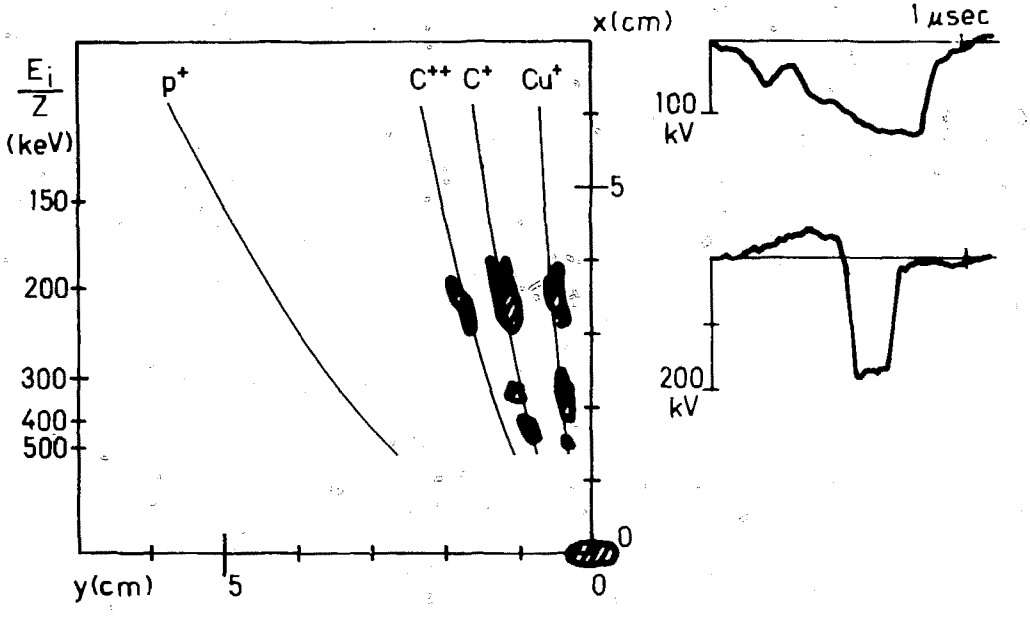
x(cm)
1 μsec
$\frac{E_i}{Z}$
(keV)
p+
C++ C+ Cu+
150
200
300
400
500
5
0
y(cm)
5
0
100
kV
200
kV

20d)

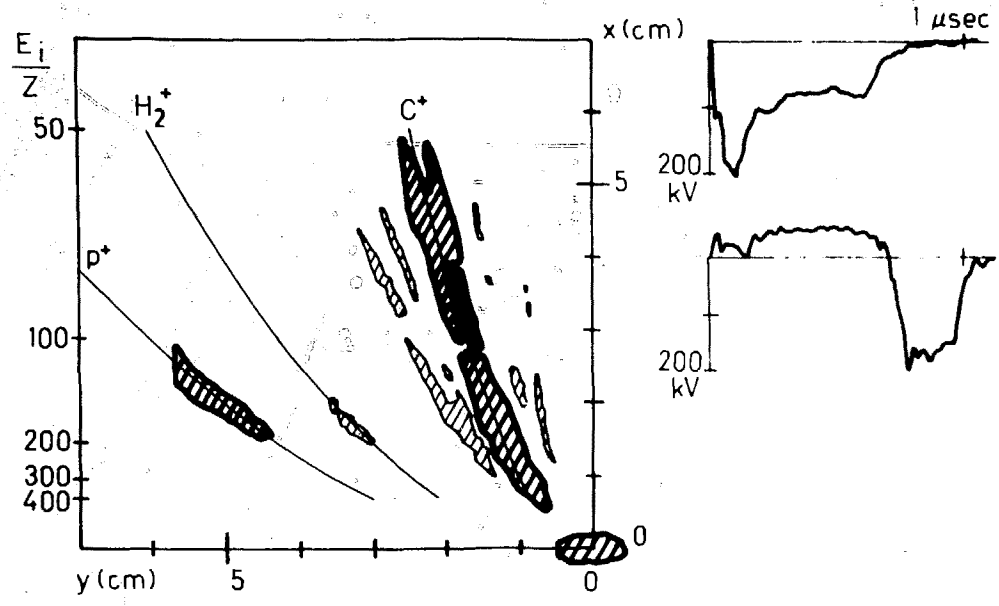
$\frac{E_i}{Z}$
50
100
200
300
400
H_2^+
C^+
p^+
x (cm)
5
0
y (cm)
5
0
1 μsec
200 kV
200 kV

20e)

through the background gas are predicted to be (C° : 0.56, C^+ : 0.37, C^{++} : 0.05) at 100 keV, (C° 0.33, C^+ . 0.52, C^{++} : 0.14) at 200 keV, and (C° : 0.10, C^+ 0.56, C^{++} 0.34) at 400 keV. It would thus be expected that in equilibrium most of the C^{++} ions from the injector were converted to C° or C^+ before reaching the mass spectrometer. It is probable that the ions approached these equilibrium fractions. Charge transfer cross sections are a maximum at the ion velocities in question, ranging from 1 to 5 $\overset{02}{A}$. A background gas pressure of only 0.2 microns or greater would have made the mean free path less than the drift distance. Such pressures were probably present in the glass drift tube which was remote from the vacuum pump. During transport to the mass spectrometer, a large fraction of the C^{++} ions was converted and appeared as the high energy component on the C^+ lines. The mass spectrometer thus showed the attainment of twice the electrostatic voltage by doubly ionized particles.

The signatures in the mass spectrometer output were clearly changed by varying the wave form of the accelerating voltage, as shown in Figure 20(b). In this case, a shunt capacitor was incorporated into the injection gap circuit. The voltage overshoot was eliminated; the voltage pulse rose steadily in time with an almost triangular profile. The maximum voltage was about 120 kV. The mass spectrometer showed a general reduction in the energy of the incident ions. This voltage profile was also used in conjunction with operation of the post-acceleration gap. The lack of the initial voltage overshoot made it possible to identify unambiguously the higher energy ions from the second gap. Such as case is shown in Figure 20(c). The post-acceleration gap was activated 830 nsec after the injector gap. The propagation time for carbon ions to travel between gaps was about 600 nsec, so that the ions arriving at the second gap during the voltage

pulse had passed through a potential of about 50 kV. The post-acceleration pulse was 175 kV over 280 nsec. The mass spectrometer plate voltage was high for these tests (2000 V) to display better the high energy ions. the low energy ions at the injector energy are off screen. The areas of detected ions are better defined than those of Figure 12(a) and (b). This was because the relatively flat post-acceleration voltage pulse resulted in a small spread of energy among the higher energy ions. There was a C^{+} area from 190 to 220 keV and a C^{++} signal from 380 to 440 keV. There was also a signature of charge exchanged C^{++} ions on the C^{+} line from 310 to 440 keV. These levels were in good agreement with an addition of the electrostatic voltages applied multiplied by the charge state of the ions. In null tests, these high energy ion signals disappeared when the second gap was not activated.

The mass spectrometer was also used in experiments with the proton injector. As expected from previous measurements, there were additional components in the beam besides protons. Data from a shot using the proton injector are shown in Figure 20(d). Also shown is the original photographic spectrometer output in Figure 20(e). There were a variety of species with Z/A less than unity, with the brightest concentration around the position of C^{+}. Most important, there was a strong proton signal that was absent when using the carbon plasma guns. There was a weak H_2^{+} signal. There are a number of interesting features in Figure 20(d). The proton and H_2^{+} signals indicate a maximum energy of 180 keV, whereas carbon-like ions were detected up to 350 keV. This may have been due in part to the previously discussed process of charge exchange of C^{++}. Another possible cause of the energy difference was the relative timing of the post-acceleration gap voltage pulse with respect to the injector. Taking into account the time

of ion propagation between gaps, an inspection of the relative voltage pulses showed that the protons arriving at the post-acceleration gap during the pulse had an energy less than 30 kV. The maximum energy of protons thus was determined mainly by the second gap, which ran at about 175 kV. The carbon ions had a longer transit time, so the ones arriving during the second gap voltage pulse were produced at higher voltage (> 100 kV) in the injector.

High energy protons were observed if the gap firing delay was adjusted properly. Such a case is shown in Figure 21. The flat voltage pulse of the second gap was used in conjunction with a time-of-flight detector 35 cm downstream to measure the velocity of the post-accelerated ions. The injector and post-acceleration voltage waveforms are displayed in Figure 21 on the same time scale as the time-of-flight probe signal. The enhancement of the ion current density following the second gap voltage pulse could have been caused by a number of factors. These include the summation of current density as the high energy ions overtook the low energy flux, electrostatic focusing effects, and possibly a decrease in space charge effects in the second gap since the average ion density was lowered during the voltage pulse. A number of shots were taken with second gap voltages of about 160 kV and a relative gap delay time of 600-700 nsec. This implied that protons arriving at the second gap had an energy of about 100 keV at the time of the second gap voltage pulse. In these shots, the average delay time between the application of the post-acceleration voltage and the arrival of the head of the ion beam was about 50 nsec, implying a velocity of 7×10^8 cm/sec. This corresponded to 260 keV protons, in agreement with the addition of gap voltages. There was no carbon signature observed in the time-of-flight detector signals under these conditions. This was because carbon ions in the gap would have originated at a time when the constantly

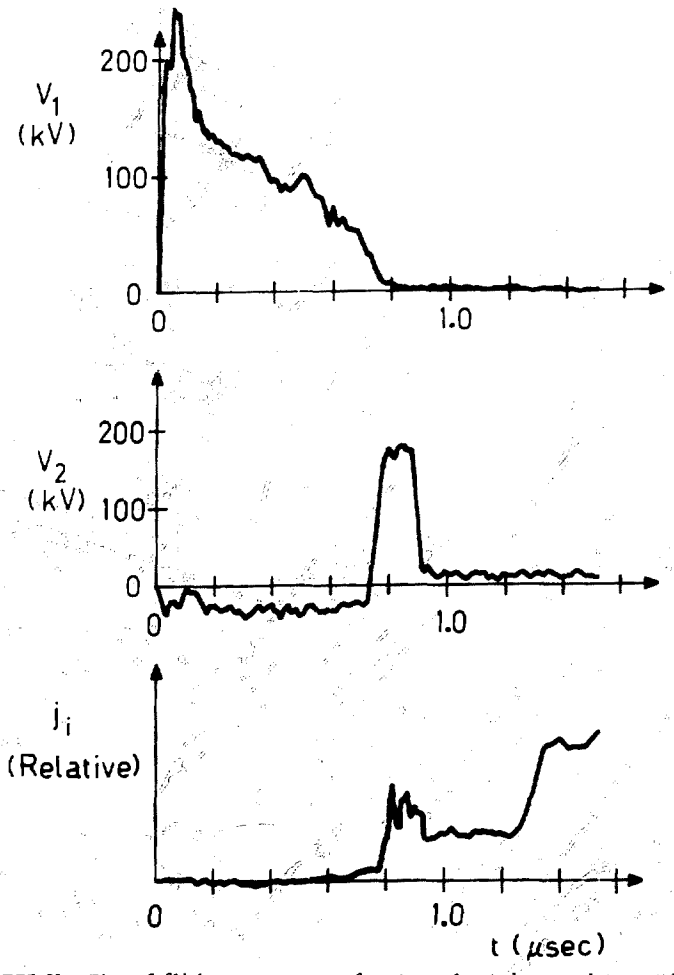

FIGURE 21 Time-of-flight measurements of post-accelerated proton beams. a) Injector gap voltage waveform showing time of origination of protons arriving at second gap during voltage pulse. b) Post-acceleration gap voltage waveform. c) Ion current density signal from charge collecting probe located 35 downstream from the second gap.

rising injector current was low. If the relative firing delay between gaps was increased to 1 μsec, the delay to the arrival of the head of the beam at the time-of-flight detector increased to from 160 to 220 nsec, corresponding to carbon in the 200 keV range. This came about because the protons from the injector pulse had already passed, and carbon ions from the high current portion of the injector pulse were allowed to propagate to the second gap before activating the voltage. This behavior was consistent with the mass spectrometer data of Figure 20(d).

High current post-acceleration experiments were performed with a carbon ion beam using the three slot injector and a 30 cm intergap spacing. As described in Section IV, probe measurements showed total currents exceeding 2 kA in this geometry. Because of noise pickup on in-vacuum current monitors, it was not possible to measure directly the current passing through the magnetically insulated gap. Nevertheless, it was possible to make a good estimate of current flow and to observe directly energy transfer to the beam by inspection of the second gap voltage waveforms with the addition of ion current. Such data are shown in Figure 22. In this case, the second Marx generator was connected directly to the gap through a 120 nsec length of 50 ohm high voltage cable. During the first 240 nsec of the voltage pulse, this circuit acted as an ideal 50 ohm transmission line. This line was charged to about 80 percent of the open circuit Marx generator voltage because of the presence of a series damping resistor. The four examples of Figure 22 were taken with varying delay times for the initiation of the post-acceleration gap. In the first, the delay was short so that no carbon ions were able to reach the gap. After an initial step associated with the erection of the Marx generator, the voltage rose to 230 keV when the Marx generator voltage was 280 kV. This indicated an open circuit at

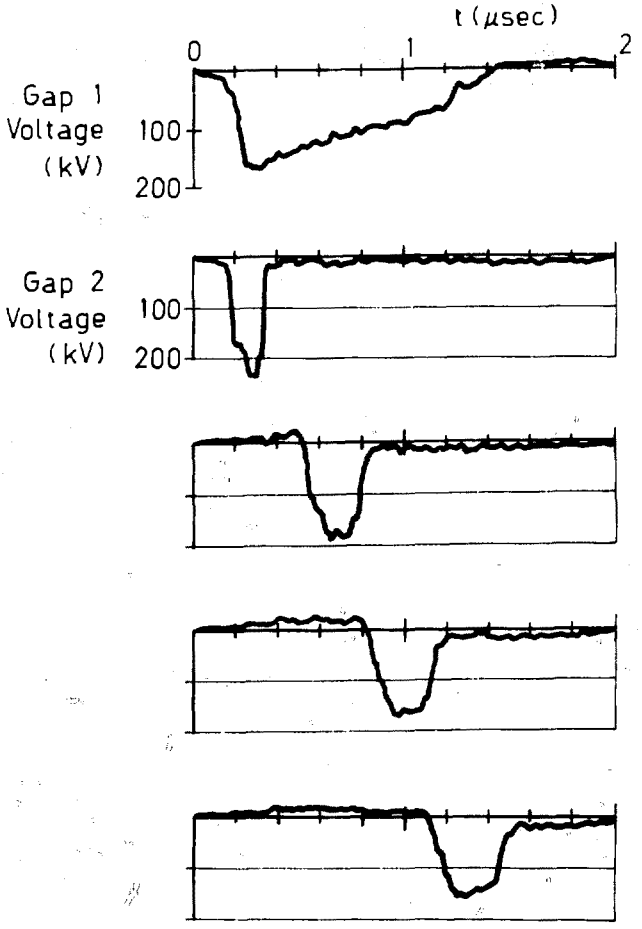

FIGURE 22 Post-acceleration of high current carbon beams. Three slot carbon injector with 30 cm intergap spacing. Voltage waveforms of second gap with beam loading varied by changing relative firing delay.

the gap. As the delay was increased, the voltage level decreased to a minimum of about 140 kV, implying a 1.8 kA load on the 50 ohm line. This was in good agreement with previous probe measurements. It is also noteworthy that the loaded voltage was flat until the crowbar, indicating a constant current level in the source limited mode.

VI. FOCUSING OF ION BEAMS IN A POST-ACCELERATION GAP

One of the major goals of our linear accelerator studies is the demonstration of the electrostatic confinement of ion beams using shaped accelerating fields. In this section, we will review the experimental evidence for magnetically insulated electrostatic lens effects in the post-acceleration gap. Such effects (coupled with the modification of electric field distributions by electron space charge) have already been discussed in regard to the injector. The presence of a virtual cathode and the strong differences between ion orbits in the one and three slot injectors are two examples. The general concept of electrostatic confinement of ions in subsequent gaps can be understood by referring to Figure 1. The shaped magnetic field lines influence electron motion resulting in curved equipotential lines concave toward the positive electrode. The transverse components of the acceleration field will thus act to keep the beam confined to an annulus. It is not necessary that the transverse field components have an accurate linear variations away from the annular axis. Studies of transverse beam dynamics indicate that non-linear confinement systems can preserve beam quality and may even have some advantages over linear systems with regard to parametric instabilities.

There were a number of possible methods for changing the curvature of the magnetic field lines and thus the focusing properties of the post-acceleration gap. These included changing the coil positions, changing the

relative currents of upstream and downstream coils, and selectively placing conducting field excluders to produce image currents. The method we chose for this experiment was to maintain a well-measured field configuration (as in Figure 1) and vary the curvature by moving the effective position of the acceleration gap. This was effected by adjustable gap trimmers, thin (0.03 cm) stainless steel hoops that protrude into the space between the main drift tube structures. There was latitude to locate the 0.7 cm acceleration gap anywhere in the 2.5 cm space between drift tubes. The field line shapes could be approximated in terms of a radius of curvature with respect to the average radius of the drift space annulus. The values that were used in experiments were +6 cm, +15 cm, -40 cm and 0 cm. Positive values are defined to be concave upstream, as shown in Figure 1. These values are subject to wide variation, since they were subjectively estimated from print-out of computer calculations of the gap magnetic field. In the paraxial approximation, it is straightforward to calculate a single particle focal length in terms of the radius of curvature of the magnetic field line with respect to the annular axis, R. It is assumed that the shape of the gap follows that of the magnetic field lines, and that the direct focusing effects of the magnetic fields can be neglected. If the beam enters the gap with energy E_B and the gap has an applied voltage V_o with transverse electric field components that can be approximated as $E_\rho \simeq (\rho/R_\ell)(V_o/d)$ (where d is the gap spacing and ρ is the distance from the average annular radius) then the electrostatic focal length is

$$f_{e.s.} \simeq \frac{R_\ell}{(1 - (E_B/(E_B + ZeV_o))^{1/2})} \qquad (4)$$

In the equation, Z is the charge state of the ion. Note that the focal length is independent of the mass, so that all singly ionized species in the beam will be deflected similarly. With a mixture of charge states (as with the carbon injector with C^+ and C^{++}) the focusing effects will still be the same since E_B is proportional to Z.

Measurements of radial focusing of the beam were performed using thin sheets of Pilot B scintillator as image detectors. The scintillators were located in the annular drift space downstream from the post-acceleration gap and could be moved longitudinally. An aperture plate was fixed 2.5 cm downsteam from the gap. There were eight apetures in the form of 0.3 cm wide slots extending across the radial extent of the drift space. The scintillators were photographed from downstream by an integrating camera. The beam image was separated from injector light shining through the aperture by rotation in the magnetic fields. Typical results are shown in Figure 23. In the experiment, the proton injector was used in combination with a floating 70 nsec Blumlein line for the second stage voltage. The scintillators were 7.6 cm below the second gap. The gap trimmer placement subtended magnetic field lines with strong curvature (R_ℓ = 6 cm). In the shot of Figure 23(a), the injector was fired with a shorted post-acceleration gap with magnetic field only. In the original photograph, there was a dim, radially uniform region of excitation from the low energy injector ions. There was considerable azimuthal width due to the spread in ion energy. In the second shot (Figure 23(b)), the post-acceleration gap Blumlein line was charged and fired with the timing shown. The voltage pulse was about 250 kV, and the entering protons had energies of 90-100 keV. A bright spot appeared on the scintillator indicating the presence of high energy ions. The spot exhibited less average rotation than the shot with injector only,

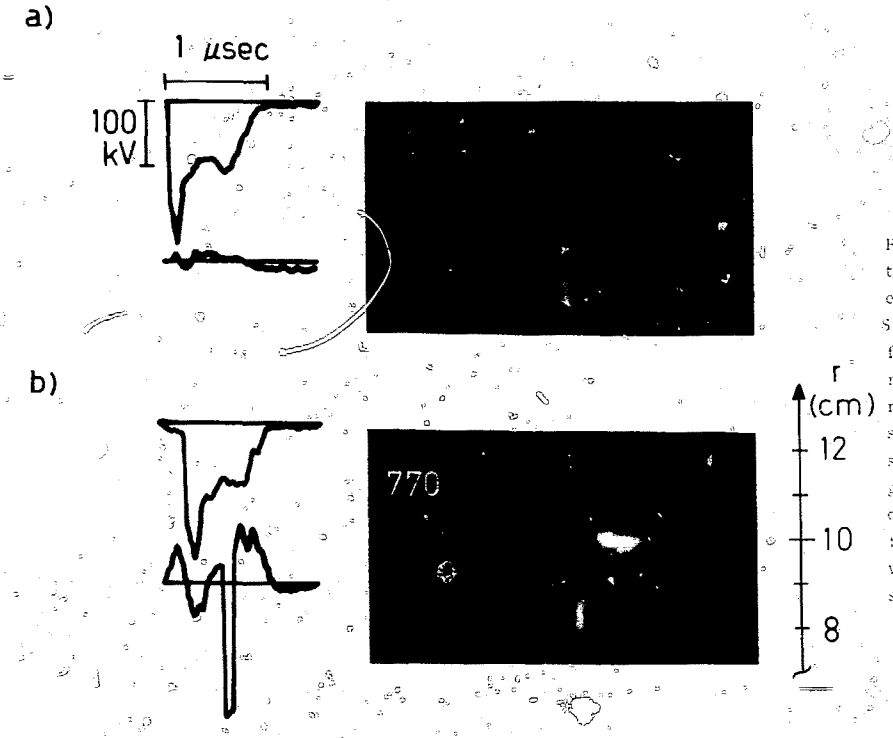

FIGURE 23 Post-accelera tion of proton beam; electrostatic focusing. Shown are voltage wave-forms for both gaps and reproductions of the response of a scintillator sheet 7.6 cm from the second gap. a) 1st second gap voltage. Very little excitation, no radial focusing. b) Second gap voltage as shown. Bright, sharp ion focus appears.

another indication of energy gain. Of greatest interest was the fact that the ions were radially focused to a sharp line at the average annular radius. The quality of this focus was dependent on the relative voltages of the two gaps, the magnetic field geometry in the acceleration gap, and the position of the detector. Another interesting feature of the shot of Figure 23(b) is the relative absence of the operation of the post-acceleration gap. The large spreading of the plasma line charge density. This was in contrast to previous short pulse experiments using the inductor gap with a flashboard gun source. Considerable effort was put made to suppress prepulse. In that case, premature activation of the flashboard often caused shorts during the main pulse.

Further tests with the pinch injector were performed with the second gap operated directly from the Marx generator. The pulselength was about 2.0 μsec. As above, the system had a 60 cm intergap spacing. Typical results are shown in Figure 24. The parameters of the acceleration gaps were maintained constant and the scintillator longitudinal position was varied. A radial focus was clearly visible at about 10 cm downstream from the second gap. This position was in agreement with the prediction of Eq. 2. Taking R_0 = 6 cm, E_B = 80 keV, and V_0 = 200 kV, Eq. 2 predicts an electrostatic focal length of 11 cm. Scaling tests were also performed by changing the voltage of the second gap and the energy of the incoming ions from the first gap. The latter was most easily accomplished by changing the relative delay of the gap activation. With the scintillator maintained at a constant position, the effect of these variations was evident.

Another variable parameter was the curvature of the magnetic field lines. Longitudinal scintillator scans clearly showed a lengthening of the focal length of the gap with a decrease in the curvature of the magnetic

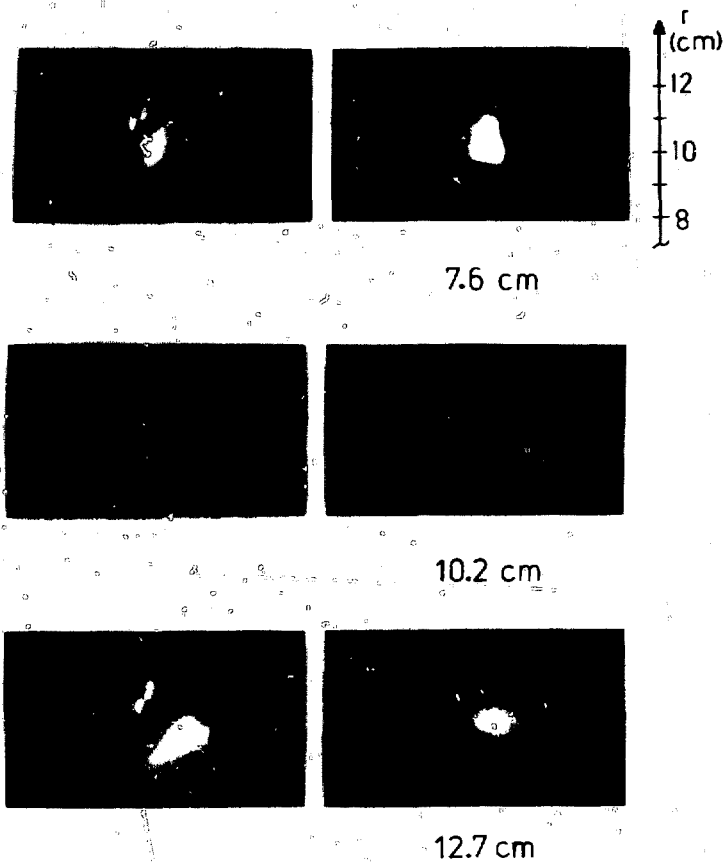

FIGURE 21 Scintillator data: proton beam post-acceleration. Variation of scintillator position with other system parameters maintained constant. Predicted electrostatic focal length is 11 cm.

field lines. The case with neutral field line curvature showed no focusing, as expected. The neutral geometry was also used in tests using the three slot carbon injector with an intergap spacing of 30 cm. In shots with no post-acceleration pulse, the low energy ions from the injector made a dim activated area on the scintillator. This was spread out considerably in azimuth because of the large energy spread of the beam. When the second gap was fired, a thin, radially uniform line with very little azimuthal displacement was observed. The scintillators were also used to demonstrate the addition of energy at the carbon beam in the post-acceleration gap. A large scintillator sheet was located 15 cm downstream from the second gap with no aperture plate. Without the post-acceleration voltage, no luminosity was observable from the scintillator, whereas it was uniformly illuminated with the application of the second gap voltage.

Probe arrays were used to identify the time-dependent focusing of the ion beams. Experimental traces are shown in Figure 25 for tests made with the proton injector with 60 cm intergap spacing. The 200 nsec voltage pulse occurred about 670 nsec after firing the injector. The incoming protons had about 80 keV energy, the second gap voltage was 200 kV, the field line radius of curvature was 6 cm, and the probes were located 10 cm downstream. The array consisted of three biased charge collectors at radii of 9.5, 10.0 and 10.5 cm. As shown, there was an evident increase in detected current density. The signal during and just proceeding the pulse are shown. The radial integral of current density was the same in both case, but the ion flux was strongly concentrated on the average radius of the annulus during the voltage pulse. This behavior was consistent with the presence of virtual electrodes and the diffusion of electrons into the acceleration gap. In this case, ions arrived at the gap well before the

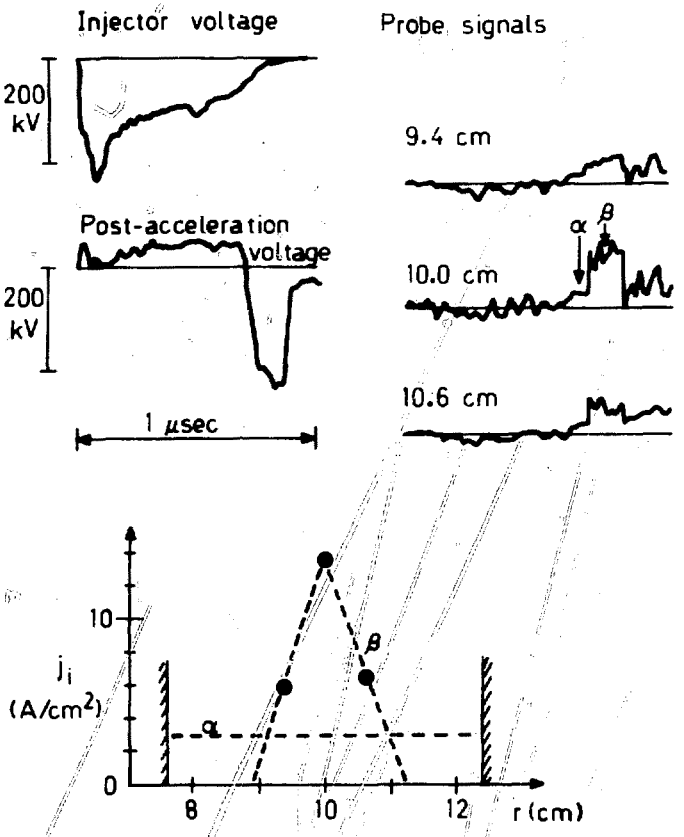

FIGURE 25 Electrostatic focusing of proton beam measured by charge collecting probe array. Probes 10 cm downstream from second gap.

voltage pulse. They were probably initially hindered from crossing the gap by space charge effects, but electron diffusion relieved this hindrance and the downstream current density rose, as shown in the probe signals. When the gap was fired, there was already a plasma prefill. The post-acceleration actually lowered the downstream ion density, so there should have been an abundant supply of electrons trapped on field lines in the gap and filling the downstream drift region. The ion motion, in this case, was determined mainly by the virtual electrode shaping, producing the sharp focus shown. The net current across the gap did not change since it was limited by the flux of ions from upstream.

The relative response of the probes was clearly changed when the gap geometry was varied. Tests with carbon beams using the neutral curvature geometry gave at most 25 percent changes in the probe response at a 15 cm distance. In some cases there was a slight focus observed, very mild compared to the situation with strong magnetic field line curvature. Probes 1.5 cm from the average beam radius actually showed a decrease in current density during the post-acceleration pulse.

VII. CONCLUSIONS

To conclude this paper, we will summarize what we feel are the significant aspects of the experiments reported. Although the results to date are not definitive, they do provide an initial basis for assessing the feasibility of high current linear accelerators in the multi-kiloampere regime. We are presently working on a number of areas that should advance the understanding of the acceleration of neutralized beams. Preliminary results have been obtained from a two-dimensional particle simulation model of a Pulselac gap. These confirm the concepts of automatic electron neutralization and the formation of virtual electrodes. A five stage, high gradient injector is

nearing completion. This has been designed to produce beams in the MeV range. This system will provide an opportunity to study transverse confinement by electrostatic lenses and the growth of longitudinal instabilities. Additionally, the multi-kiloampere, high quality beam that should be obtained will be useful for basic studies of neutralization, beam focusing, and vacuum transport.

We have made a number of advances in the technology of high flux ion injectors. The radial magnetic field geometry with independent plasma injection has a number of advantages over previous intense ion beam injectors. There is the ability to choose the ion species by means of the plasma gun. Since the plasma flux controls the injector current, the injector can operate in an enhanced current density mode while maintaining high efficiency and controllable impedance. Constant current operation for pulselengths approaching a microsecond were obtained at the 2-3 kA level. The injector has the potential for high repetition rate operation for a large number of shots without maintenance. Also of importance is the fact that we were able to improve the optics of the beam considerably by electrostatic field shaping. The properties of the injector used in these experiments are not far removed from the requirements for a fusion reactor high current linear accelerator.[2] An accelerator module would produce about 100 kA in a 30 nsec pulse at the output. This would be achieved by a combination of beam acceleration and bunching using ramped voltage waveforms. If the injector operated at a microsecond pulselength, it need only produce 3 kA. An angular divergence of about 1° is suitable. We have already demonstrated the ability to produce carbon beams. Since the ion species is determined by the plasma gun, it is probable that we can produce a wide variety of intermediate mass ion species.

The present experiments indicate that a highly effective beam neutralization process is taking place. An upper limit on the ion-electron charge imbalance is 0.2 percent. The question of whether this process is the one we have described theoretically must be resolved by additional experiments. The post-acceleration of the beam appears to take place classically. The ions emerge with an energy given by the sum of the electrostatic voltages on the gaps. The potential of the beam appeared to be closely clamped to the potential of the surrounding drift tube. This result is in keeping with the concepts of electron conduction across field lines to the beam volume. Using two gaps, carbon and proton beams exceeding 2 kA were accelerated to 250-300 keV. Approximately one half the current density in the carbon beams corresponded to C^{++} ions, and these were accelerated to over 500 keV.

We have demonstrated electrostatic deflections of ions in a post-acceleration gap. These deflections were in agreement with calculated values and appeared to be controlled by the curvature of applied magnetic field lines and electron space charge effects. Radial compression of the ion current density by over a factor of five was detected. The post-acceleration gap used in these experiments was a special case of the general class of magnetically insulated electrostatic lenses. In comparison to simple electrostatic lenses, the addition of magnetic insulation serves two purposes. It allows the application of very high field stress, and it makes it possible to apply deflecting fields across the entire cross section of the beam. This would not be possible for high current beams in a simple electrostatic lens, since the Debye shielding distance for typical beams used in this experiment was sub-millimeter. The experimental results allow some optimism about both the electrostatic focusing of ion beams in a high

current linear accelerator and the potential for general magnetically insulated electrostatic lenses. These lenses can be configured to deflect ions to the system axis for final focusing applications in an inertial fusion reactor.

ACKNOWLEDGEMENT

We would like to thank Mr. M. Wilde for his many contributions to the design and operation of the experimental apparatus. This work was supported by the U. S. Department of Energy, under Contract DE-AC04-76-DP00789.

APPENDIX I. CALCULATIONS OF THE MAGNETIC FIELD AND SINGLE PARTICLE ION ORBITS IN THE PULSELAC GAP

The magnetic fields of Figure 1 were calculated numerically using a Poisson's equation solver. It was based on a fast Fourier transform in the z direction followed by a single cyclic reduction in the r direction. Effects of the coils as well as a conducting boundary at the outer radius were included. The same code was used to calculate single particle paraxial ion orbits in the applied magnetic field. The variation of B_r with radius in a typical location of the acceleration gap is shown in Figure 26(a). The field magnitude was highly non-uniform. In addition to a general fall-off with radius, there was a dip at the average annular radius caused by bulging of the field lines between the coil sets. Because of these opposing effects, the field magnitude did not change greatly between the average radius and the outer radius of the gap. This field value, the minimum in the gap, was used as the scaling value $\overline{B}_r$. It ranged between 2.5 and 3.8 kG in the experiments.

The gap magnetic fields have three effects on particle orbits: 1) the radial fields induce an azimuthal velocity when passing through the gap, 2) this azimuthal velocity gives the beam a net rotation, and 3) the combination of B_r and B_z fields near the coils act as solenoidal lenses to give radial deflections. These effects can be written as

$$\frac{v_\theta}{v_z} = \frac{f_1(z)\,\overline{B}_r}{A^{1/2}\,E_B^{1/2}} \quad , \qquad \text{(AI-1)}$$

$$y = f_2(Z)\ \bar{B}_r\ /\ A^{1/2}\ E_B^{1/2} \quad , \qquad \text{(AI-2)}$$

$$\frac{v_r}{v_z} = \frac{f_3(z)\ \bar{B}_r}{A^{1/2}\ E_i^{1/2}} \quad . \qquad \text{(AI-3)}$$

In these equations, $\bar{B}_r$ is in kG, A is the mass number of the ions, E_B is the beam energy in MeV, and y (the azimuthal deflection) is in cm. The functions $f_1(z)$, $f_2(z)$, and $f_3(z)$, derived from the computer calculations, are plotted in Figure 26(b), (c), and (d), respectively. The functions $f_1(z)$ and $f_2(z)$ pertain to particles entering the gap at the average annular radius (10 cm) with initial velocity in the z direction only. Note that in Figure 27(a) the ion gains no net azimuthal velocity in passing through the double gap as expected. There is a net azimuthal deflection shown in Figure 26(b) even though there is no acceleration in the gap. This comes about because of the asymmetry of the coil sets (see Figure 1). These graphs can also be used if there is acceleration if the gap is considered to be narrow. The particle orbit can be calculated from z = 0 to the gap location using the initial energy, and from the gap to 20 cm with the higher beam energy.

The radial deflection function, $f_3(z)$, is shown in Figure 26(c) for a 7.6 cm radius. This deflection came about from an interaction of the induced azimuthal velocity with the longitudinal field components, $v_\theta \times B$. The deflection is highly non-linear with distance from the annular axis. The general effect of the fields is to focus particles towards the average radius.

FIGURE 26 Magnetic field calculations for Pulselac gap. a) Variation of B_r with radius in gap. b) Function $f_1(z)$, giving azimuthal velocity (see text). c) Function $f_2(z)$, giving azimuthal displacement. d) Function $f_3(z)$, giving radial velocity.

26
a)

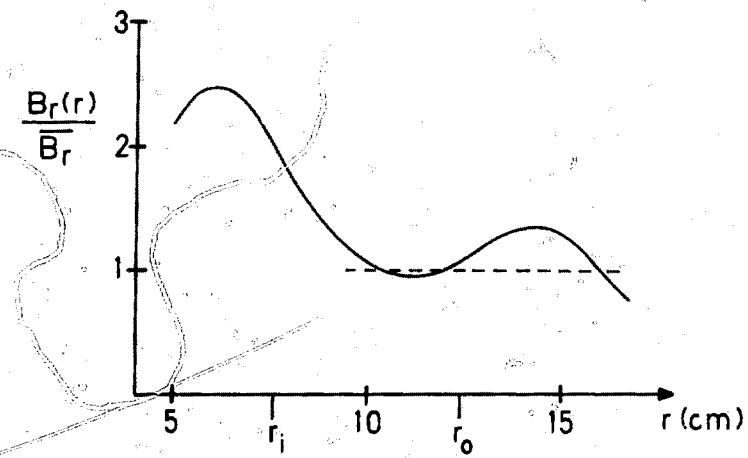
3
2
1
$\frac{B_r(r)}{\overline{B_r}}$
5
r_i
10
r_o
15
r (cm)

26
b)

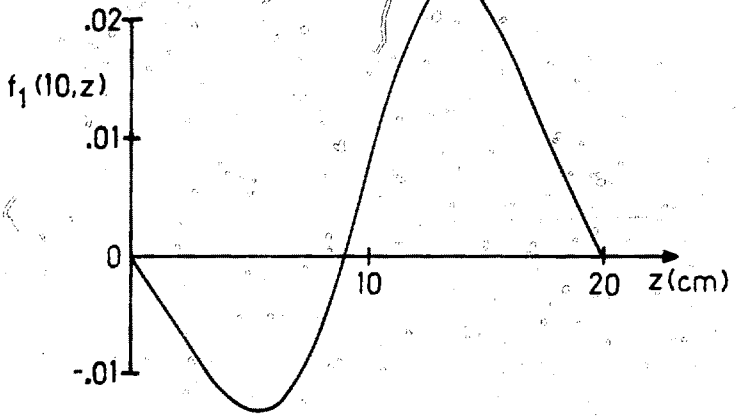
.02
.01
0
-.01
$f_1(10,z)$
10
20
z(cm)

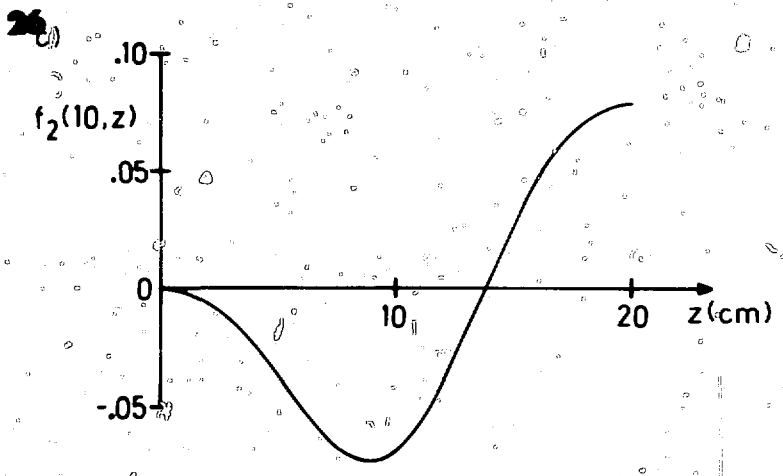
.10
$f_2(10,z)$
.05
0
-.05
10
20
z(cm)

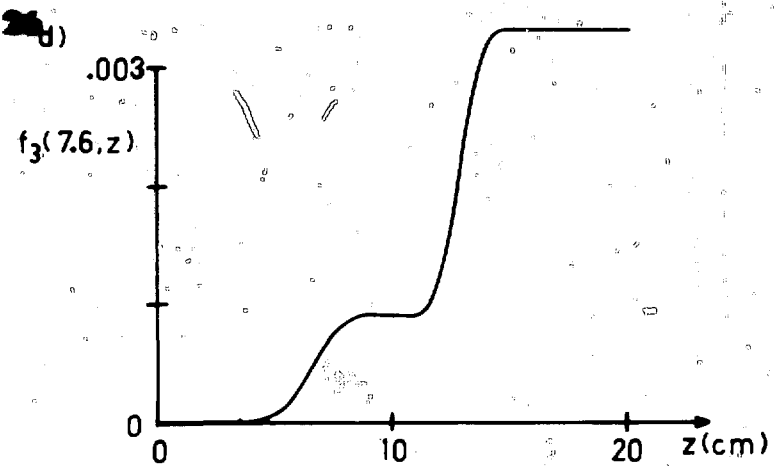
.003
$f_3(7.6,z)$
0
0
10
20
z(cm)

We conclude with examples of the magnitude of the magnetic effects for parameters typical of the experiments. The induced azimuthal velocity had little effect on beam propagation since the self-generated magnetic fields of the ions are small compared to the applied fields. The azimuthal deflections proved useful in determining the particle species extracted from the injector. In a typical set-up, an aperture array was located at about the 11.5 cm distance in Figure 26, and scintillation detectors 6.4 cm downstream. The change in f_2 was about 0.13. The predicted translations at 3.1 kG were 1.1 cm for 120 keV protons and 0.3 cm for C^+. These predictions were in good agreement with scintillator or damage plate measurements taken with the two injectors.

The radial deflections could have been a significant effect for protons emerging from the injector. The inside radius of the flashboard injector was 9 cm. On this radius, the change in f_3 from 9 to 20 cm is about 5×10^{-4}. With $\bar{B}_z$ = 3.1 kG and 120 keV protons, the angular deflection is 2.3°, comparable to the beam divergence. For C^+ at the same energy, the deflection is less than 1°. The solenoidal lens effects would decrease in importance with post-acceleration as $E_B^{-1/2}$. The azimuthal translations would also decrease accordingly.

APPENDIX II. ION BEAM LOSSES AND SECONDARY ELECTRON PRODUCTION

In most intense ion beam experiments involving propagation through vacuum, the source of neutralizing electrons appears to be secondary emission processes. A portion of the beam strikes surrounding conducting boundaries until there are sufficient electrons for neutralization. The secondary emission coefficient (γ) is high at the beam energies typically used (0.1 to 1 Mev). In this Appendix, we will calculate what fraction of beam ions must be lost to produce electrons in order to satisfy charge balance, without inquiring into the detailed dynamics of ion losses. This will give at least a rough idea of the circumstances under which secondary emission is sufficient for neutralization, and indicate regimes where active sources of boundary electrons will have a noticable effect on propagation. This is particularly important for neutralized linear accelerator experiments, where the addition of active electron sources is planned.

The beam is assumed to propagate in a region surrounded by conducting walls, as shown in Figure 27. The only source of neutralizing electrons is taken to be secondary emission from ion collisions with the walls, characterized by an average coefficient γ (number of electrons produced per incident ion). Three additional simplifying assumptions are 1) the beam has uniform density in the transverse direction, 2) all ions have the same velocity, v_z, and 3) electrons do not move in the longitudinal direction. The third assumption is rigorously true in a region of transverse magnetic field lines.

We consider a volume element $A_b dz$, where A_b is the cross sectional area of the beam. In this element, the condition $n_e \simeq n_i$ must hold. For the high current beams considered, even a small fractional imbalance in the space charge would cause extremely large electric fields. In this case,

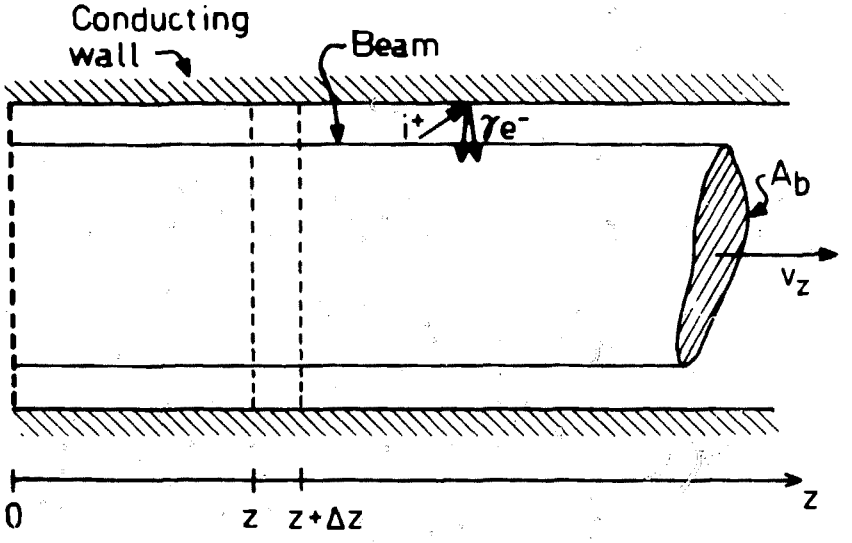

FIGURE 27 Geometry for calculating minimum losses of ion beam to assure adequate supply of secondary electrons for neutralized, vacuum propagation.

the following conservation equation can be written for the ion beam density:

$$\frac{\partial n_i}{\partial t} \Delta t \, A_b dz = [n_i(z) v_z A_b - n_i(z + \Delta z) v_z A_b] \Delta t$$

$$- \frac{\partial n_i}{\partial t} \frac{1}{\gamma} \Delta t \, A_b dz \quad . \tag{AII-1}$$

The left hand side of the equation is the change in the number of ions in the volume element in time Δt. On the right hand side are two terms representing the factors that change the ion density. The first term is the standard convection expression, while the second represents the number of ions that must be lost to the walls to produce sufficient electrons to balance the change of ion density in the element. The wall loss term is included only when $\partial n_i/\partial t \geq 0$. When $\partial n_i/\partial t < 0$, electrons simply flow back to the walls to match the decreasing ion density. The following equation describes the propagation of ions when secondary emission is necessary for neutralizations:

$$\frac{\partial n_i}{\partial t} + \frac{v_z}{(1 + 1/\gamma)} \frac{\partial n_i}{\partial z} = 0 \quad \text{when} \quad \frac{\partial n_i}{\partial t} \geq 0 \tag{AII-2}$$

This has the form of the standard convective equation with a modified propagation velocity, $v_z^* = v_z(1 + 1/\gamma)$.

This result has the following interpretations. If γ is very large, then beam propagation is unaffected by electron production. If there is a specified $n_i(0,t)$ at $z = 0$, then at a downstream location $n_i(z,t) = n_i(0, t - z/v_z)$ if beam divergence is neglected. On the other hand, with a finite value of γ and with $n_i(0,t)$ rising monotonically or constant, the equation

$n_i(z,t) = n_i(0,t - z(1 + 1/\gamma)/v_z)$ holds. To illustrate the implications of this result, we consider a pulse of ions injected at $z = 0$ such that $n_i(0,t) = n_{io}$ for $0 < t < t_p$, and $n_i(0,t) = 0$ for all other times. The rise in ion density arrives at the location z_o at time $z_o(1 + 1/\gamma)/v_z$. The fall of the ion density propagates at the velocity v_z since a beam of decreasing density is unaffected by electron production. Thus, the pulse terminates at $z_o/v_z + t_p$. The net loss of ions per unit cross section area is found to be $n_{io}z_o/\gamma$, which is the number needed to produce a density of electrons equal to n_{io} from 0 to z_o. The fraction of the beam transported is $(1 - (z_o/v_z)/(\gamma t_p))$. This result suggests a rough criterion for conditions under which secondary electron emission is sufficient to allow ion beam propagation. Electron production effects are negligible when $(z_o/v_z)/\gamma t_p \ll 1$, or when the delay time of the point of observation divided by the secondary emission coefficient is small compared to the beam pulselength. In the experiments of this paper, 120 keV carbon ions propagated over the 30 cm intergap spacing in about 200 nsec. The secondary emission coefficient is unknown, since we do not know the angular distribution of ions striking the wall, but it is quite probably greater than unity. Thus $(z/v_z)/\gamma t_p \ll 1$, and we conclude that with pulselengths on the order of a microsecond, it is unlikely that electron production effects could be distinguished from other processes.

REFERENCES

*Laboratory of Plasma Studies, Cornell Univesity, Ithaca, NY.

**Department of Chemical and Nuclear Engineering, University of New Mexico, Albuquerque, NM.

1. S. Humphries, Jr., J. Appl. Phys. 49, 501 (1978).
2. S. Humphries, Jr. J. W. Poukey and G. Yonas, Collective Methods of Acceleration, edited by N. Rostoker and M. Reiser (Harwood, Academic Pub., New York, 1979), 595.
3. S. Humphries, Jr., G. W. Kuswa and J. W. Poukey, Proc. Particle Accelerator Conf. (San Francisco, 1979), IEEE Trans. Nucl. Sci. NS-26, 4220 (1979).
4. J. W. Shearer, Nucl. Fusion 15, 952 (1975).
5. M. J. Clauser, Phys. Rev. Lett. 35, 848 (1975).
6. R. O. Bangerter and D. J. Meeker, Proc. 2nd Int'l Topical Conf. on High Power Electron and Ion Beam Research & Technology, edited by J. A. Nation and R. N. Sudan (Laboratory of Plasma Studies, Cornell Univ., 1977), 183.
7. F. Winterberg, Plasma Phys. 17, 69 (1975).
8. S. Humphries, Jr., R. N. Sudan and L. Wiley, J. Appl. Phys. 47, 2382 (1976).
9. S. A. Goldstein and R. Lee, Phys. Rev. Lett. 35, 1079 (1975).
10. J. W. Poukey, J. R. Freeman, M. J. Clauser and G. Yonas, Phys. Rev. Lett. 35, 1806 (1975).
11. S. A. Goldstein, G. Cooperstein, R. Lee, D. Mosher and S. J. Stephanakis, Phys. Rev. Lett. 40, 1504 (1978).
12. D. J. Johnson, G. W. Kuswa, A. V. Farnsworth, J. P. Quintenz, R. J. Leeper, E. J. T. Burns and S. Humphries, Jr., Phys. Rev. Lett. 42, 610 (Feb. 1979).

13. See, for instance, T. H. Martin, D. L. Johnson and D. H. McDaniel in Ref. 6, 807.

14. F. Winterberg, Z. Physik A 280, 359 (1977).

15. See for instance, R C. Arnold, Nature 276, 19 (1978).

16. See, for instance, A. Faltens, D. L. Judd and D. Keefe in Ref. 6, 57.

17. See, for instance, A. Faltens and D. Keefe, Particle Accelerators, 8, 245.

18. See, for instance, A. D. Vlasov, Theory of Linear Accelerators (Atomizdat, Moscow, 1965), translation (Israel Program for Scientific Translatios, Jerusalem, 1968), 72.

19. S. Humphries, Jr. and J. W. Poukey, Particle Accelerators 10, 71 (1979).

20. S. Humphries, Jr. C. Eichenberger, and R. N. Sudan, J. Appl. Phys. 48, 2738 (1977).

21. J. W. Poukey and S. Humphries, Jr., Appl. Phys. Lett. 33, 122 (1978).

22. S. Humphries, Jr., Appl. Phys. Lett. 32, 792 (1978).

23. S. Humphries, Jr., submitted to Particle Accelerators.

24. P. L. Dreike, C. Eichenberger, S. Humphries, Jr., and R. N. Sudan, J. Appl. Phys. 47 85 (1976).

25. In the carbon injector, ions were extracted from a moving plasma, a process similar to that described in M. Dembinski, P. K. John, and A. G. Ponomarenko, Appl. Phys. Lett. 34, 553 (1979).

26. S. Humphries, Jr., C. W. Mendel, G. W. Kuswa and S. A. Goldstein, to be published, Rev. Sci. Instrum.

27. C. W. Mendel, Jr., J. Appl. Phys. 42, 5483 (1971).

28. S. Humphries, Jr., Conference Record, 1978 IEEE Int'l. Conf. on Plasma Science, 78CH1357-3 NPS (IEEE, Piscataway, 1978), 115.

29. C. Eichenberger, S. Humphries, Jr., J. Msenchen and R. N. Sudan, J. Apl. Phys. 48, 1449 (1977).

30. S. Humphries, Jr. and G. W. Kuswa, Appl. Phys. Lett. 35, 13 (1979).

31. Shyke A. Goldstein, private communication, Jaycor.

32. D. J. Johnson, A. V. Farnsworth, Jr., D. L. Fehl, R. J. Leeper and G. W. Kuswa, to be published in J. Appl. Phys.

33. K. D. Bergeron, Appl. Phys. Lett. 28, 306 (1976).

34. T. M. Antonsen and E. Ott. Phys. Fluids 19, 52 (1976).

35. There are a number of possible definitions for the microscopic half angle of divergence of a beam. Since we do not have a detailed knowledge of the beam transverse distribution function, we will adopt a distribution that is convenient from the point of view of making analytic predictions of downstream spatial distributions. At every point in configuration space, the beam is taken to have a uniform distribution in angle between $-\Delta\theta_b$ and $+\Delta\theta_b$ in the x and y directions. Here, $\Delta\theta_b$ is the boundary half angle of divergence. This can be compared to the typical beam divergence parameter, $\Delta\theta_g$, which represents the 1/e half width of an angular beam distribution with Gaussian profile, if we accept the definition that beams of the same quality have one-half the total particles contained within the same angle. In this case, $\Delta\theta_g = 0.75\ \Delta\theta_b$.

36. D. J. Johnson, private communicaton, Sandia Laboratories.

37. J. M. Neri, D. A. Hammer and R. N. Sudan, Conference Record, 1979 IEEE Int'l Conf. on Plasma Science, 79CH1410-0 NPS (IEEE, Piscataway, 1979), 24.

38. S. A. Goldstein, private communication, Sandia Laboratories.

39. D. S. Prono, J. M. Creedon, I. Smith and N. Bergstrom, J. Appl. Phys. 46, 3310 (1975).

40. T. M. Antonsen and E. Ott, Appl. Phys. Lett. 28, 424 (1976).

41. J. Golden, C. A. Kapetanakos, S. J. Marsh and S. J. Stephanakis, Phys. Rev. Lett. 38, 130 (1977).

42. J. N. Olsen, G. W. Kuswa and E. D. Jones, J. Appl. Phys. 44, 5 (1973).